water

MDPI

Review

Nanocomposite Zinc Oxide-Based Photocatalysts: Recent Developments in Their Use for the Treatment of Dye-Polluted Wastewater

Abayomi D. Folawewo and Muhammad D. Bala *

School of Chemistry & Physics, University of KwaZulu-Natal, Westville Campus, Private Bag X54001, Durban 4000, South Africa
* Correspondence: bala@ukzn.ac.za

Abstract: This review highlights current developments in utilising zinc oxide (ZnO) composite materials as photocatalysts. Systematic analyses of the various synthetic methods for producing ZnO-based hetero-structured materials, the variety of methods for their characterisation, their mechanisms of action, and widespread applications for the degradation of pollutants are discussed. Structure/activity relationships and methods of improving on some of the recognised shortcomings of ZnO-based nanomaterial catalysts are also presented.

Keywords: nanocomposite; water purification; visible light irradiation; ZnO; dyes

Citation: Folawewo, A.D.; Bala, M.D. Nanocomposite Zinc Oxide-Based Photocatalysts: Recent Developments in Their Use for the Treatment of Dye-Polluted Wastewater. *Water* **2022**, *14*, 3899. https://doi.org/10.3390/w14233899

Academic Editor: Jesus Gonzalez-Lopez

Received: 1 November 2022
Accepted: 21 November 2022
Published: 30 November 2022

1. Introduction

Modern agricultural production, chemical and allied industries, and urban growth have contributed to contaminant discharge into natural waterways, including rivers and lakes. Industrialisation and urbanisation are the key indicators of development. However, they also serve as primary pollution sources, including many hazardous chemicals, frequently contaminating freshwater (re)sources. Water is vital and essential for the sustenance of life on earth, and only 2.5% of the available global supply is freshwater [1]. Industrial effluents (from sources as diverse as the paper, food, ink, paint, rubber, cosmetics, and textile industries) are grounds for concern because they harm ecosystems when discharged untreated into water bodies [2,3]. Large quantities of coloured wastewater from the textile and tanning industries are some of the principal contaminants of freshwater in many middle to low-income economies globally [4]. Over 1×10^5 different dyes are known globally, with over 7×10^5 tonnes produced annually [5]. The azo dye class constitutes almost 70% of this total, while anthraquinone-based ones contribute 15% of all the colour-bearing dyes used in the textile and allied industries [6]. Table 1 highlights the classification, properties, and pollutants associated with the common industrial dyes.

Dyes in water bodies can be toxic, and it is crucial to develop adequate protection protocols for surface and groundwater [7,8]. Hence, appropriately specialised and cost-effective treatment techniques for industrial wastewater are urgently needed, which is necessary before their infusion into water bodies. It is cheaper to treat at the source than to decontaminate polluted rivers, lakes, and dams, which may be difficult or near impossible to achieve [9].

Table 1. Characteristics and category of common industrial dyes [10].

Dye Class	Characteristics	Pollution Contributor
Acidic	Water-soluble anionic compounds	Colour, organic acids, unfixed dyes.
Basic	Water-soluble used in weakly bright acidic dye baths	Not applicable.

Table 1. *Cont.*

Dye Class	Characteristics	Pollution Contributor
Direct	Water-soluble, anionic compounds used without mordant	Colour, salts, surfactants, unfixed dyes, retarding agents; finish; diluents.
Dispersive	Insoluble in water	Colour; organic acids; carriers; levelling agents; phosphates; defoamers; lubricants; dispersants; delustrants; diluents.
Reactive	Water-soluble anionic dye	Colour; salt; alkali; unfixed dye;surfactants; defoamer; diluents; finish.
Sulphur	Organic compounds containing sulphur/sulphide	Colour; alkali; oxidising agent; reducing agent; unfixed dye.
Vat	Chemically complex and water-insoluble	Colour; alkali; oxidising agents; reducing agents.

The common techniques that have been used to eliminate contaminants (colour in wastewater, recalcitrant carbon-based pollutants, and those with low biodegradability) include flocculation/coagulation [11,12], sedimentation [13], ion exchange [14], use of molecular sieves [15], membrane filtration using reverse osmosis [16], membrane filtration [17], adsorption processes [4,18], ozonation [19], chlorination [20], chemical precipitation [20], and chemical/electrochemical techniques [21]. Moreover, most of these techniques require long operation times, are expensive, and produce generous quantities of toxic sludge/product, which are expensive to remove [22]. However, in the last thirty years, tremendous research efforts on water clean-up have led to the development of advanced oxidation processes (AOPs) for water purification [23]. The possibility of utilising available and sustainable sunlight-powered photochemical AOPs makes it the most favoured wastewater remediation technique. AOPs oxidise contaminants quickly and non-selectively [24]. The AOPs break down organic contaminants and destroy persistent organic compounds, especially for low biodegradable wastes using reactive oxygen species (ROS) such as the hydroxyl ($^{\bullet}OH$) and superoxide ($O_2^{-\bullet}$) radicals. These radicals are well-known ROS with 2.7 and −2.3 eV oxidation potentials, respectively [9]. The oxidation potentials of most pollutants vary from -1 to 2 eV. Therefore, an organic compound in a reactor containing ROS will either be oxidised or reduced and broken down into mostly CO_2, H_2O, and mineral acids [25–27]. In general, AOPs include chemical, built on the Fenton reaction and peroxonation; photochemical, based on H_2O_2 and O_3; photo-Fenton processes ($H_2O_2/Fe^{2+}/UV$); heterogeneous photocatalysis (semiconductors/UV); and sonochemical and electrochemical that include anodic oxidation, electro-Fenton, and associated processes [9].

Specifically, heterogeneous semiconductor photocatalysis/photocatalyst (SCP), in general, is cheap (no chemical reagents or electricity needed), green (no secondary process products), and very effective for the elimination of contaminants. SCP is a well-known method with the tremendous prospect of combating contaminants in water or air [28]. There is a growing interest in the search for efficient heterogeneous photocatalysts that include TiO_2 [29], ZnO [30], ZnS [31], ZrO_2 [32], semiconductor-graphene, perovskites [33], MoS_2 [34], WO_3 [35], CdS [36], and Fe_2O_3 [37]. ZnO and TiO_2 are non-toxic, cheap, and stable with efficient photocatalytic activity; hence, they are the most researched SCP [37]. As a result of their low cost, stability, and high oxidative ability, the use of ZnO and TiO_2 in photocatalysis has developed immensely [38,39].

An ideal photocatalyst must be inexpensive, safe, and activated by visible/solar light. Most recently, ZnO has become the SCP of choice; in fact, the photodegradation activity of ZnO (band gap of 3.37 eV) on methylene blue is four times more efficient than TiO_2 [30] under ultraviolet (UV) irradiation. ZnO is an attractive SCP for various applications [40,41] given its hardness, stability, low toxicity, optical transparency, enormous excitation binding energy (∼60 meV—which ensures efficient excitonic UV emission), and piezoelectric prop-

erties [42–44]. ZnO has been proposed as a TiO_2 replacement because of its efficient solar spectrum utilisation. Furthermore, ZnO has a higher quantum efficiency [45], with higher electron mobility [200–300 $cm^2/(V{\cdot}s)$], as compared to TiO_2 (0.1–4.0 $cm^2/(V{\cdot}s)$), coupled with the fact that it absorbs a higher portion of the UV spectrum, leading to better photocatalytic performance [41,45]. ZnO is better than TiO_2 in the photocatalytic breakdown of fungicides under sunlight irradiation [46], and other desirable properties are further highlighted in Table 2. However, the band gap of ZnO, on the other hand, does not match the wavelength of visible radiation; it occurs exclusively in the UV region. That means only a small portion of the total solar light radiation is utilised, making photocatalysis with ZnO an impracticable method at an industrial scale [23]. Hence, the effectiveness of a ZnO process is low due to the poor utilisation of visible/solar light, its large band gap, low quantum efficiency, health hazards involved in the operation of a UV plant, and fast e^-/h^+ recombination, which are all considered practical bottlenecks for its mass utilisation, thus requiring the development of more effective methods for its widespread adoption as an SCP.

Table 2. Desirable properties of ZnO in heterogeneous catalysis.

S/N	ZnO Properties	Ref.
1	Higher efficient photocatalytic activity compared to TiO_2.	[47–49]
2	High electron mobility and lifespan.	[50]
3	ZnO possesses relatively lower production costs and easy fabrication into a variety of nanostructures that include nanowires, nanoribbons, nanobelts, nanocombs, nanospheres, nanofibers and nanotetrapods.	[51]
4	There is a general reduction of the recombination of electrons and holes by the surface states as well as their high surface-to-volume ratio, ZnO nanotetrapods showed enhanced photocatalytic activities.	[49]
5	Zn based compounds are biocompatible with the functions of the human body.	[52]

Much research has been conducted to alter its structure and properties to decrease the recombination speed of the photogenerated charges and make it easily stimulated by visible light [53]. These alterations include, but are not limited to:

(i) Doping with metals and non-metals;
(ii) Coupling with other semiconductors;
(iii) Surface deposition of conducting metals;
(iv) Coupling with carbon materials.

For a comprehensive review of other wastewater treatment methods besides AOPs, see [1] and for a review of the development and fabrication of ZnO nanoparticles for wastewater treatment using visible/solar-photodegradation, especially its mechanism before 2018, see [53]. This review focuses on recent developments covering mainly the period after 2019, although for context, key background reports from earlier periods are provided where that is deemed necessary. The areas covered are the synthetic strategies, characterisation, and mechanisms of action for ZnO-based compounds applied in visible light photocatalysis. The various techniques that researchers have developed for the alteration/enhancement of the structure of ZnO to improve its properties and ability to degrade organic compounds, especially dyes, are highlighted.

To contextualise the present review, a 2020 search of SciFinder Scholar® (Chemical Abstract Service; Columbus, OH; USA) with the terms "photocatalyst + dye" returned a hit of about 9944 manuscripts covering twenty years (2001–2020). Similarly, a search with the keyword "Vis photocatalyst + dye" returned only 2386 manuscripts, and a search with "UV photocatalyst + dye" returned 1313 for the same period. This highlights a renewed interest of the scientific community in developing new Vis active photocatalysts, whereas a search of "ZnO Vis photocatalyst + dye" returned only 246 manuscripts, suggesting that the use of ZnO is under-researched as a semiconductor photocatalyst. The breakdown is shown in Figure 1.

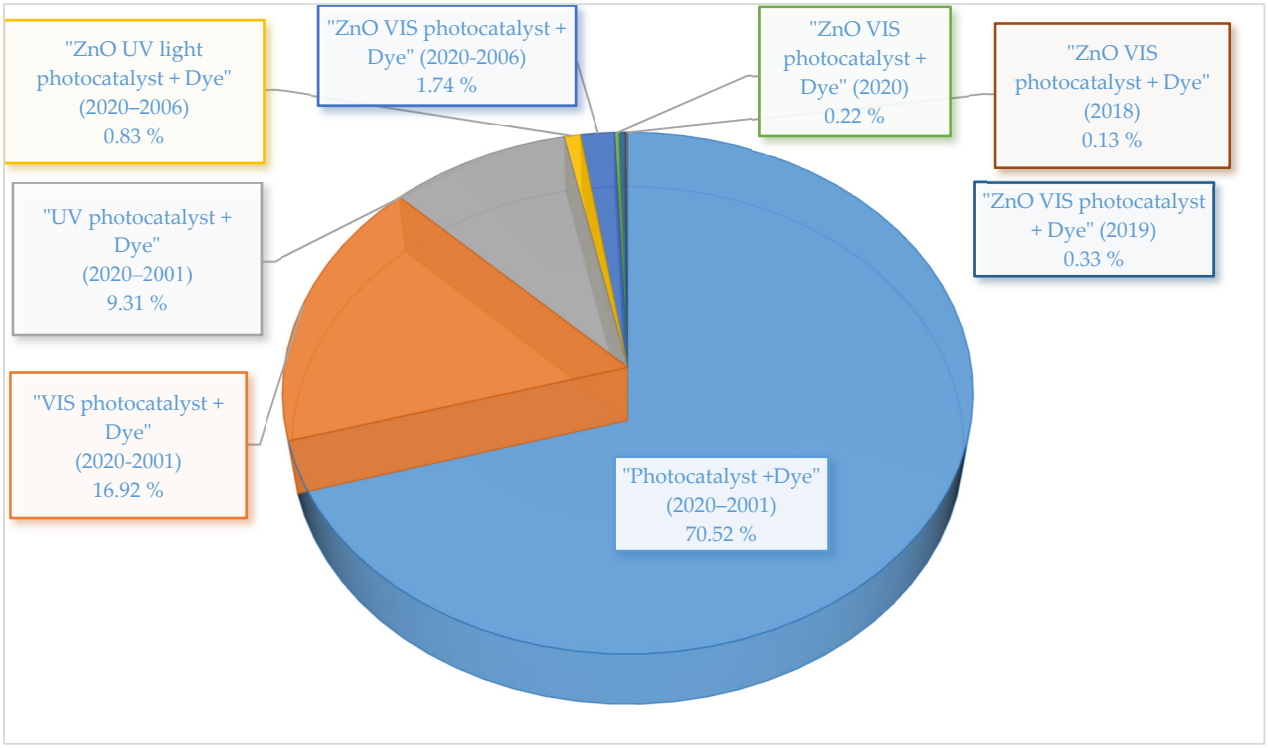

Figure 1. SciFinder Scholar® results with several "photocatalyst + dye" search keywords.

2. Synthetic Strategies for the Preparation of ZnO Nanocomposites for Improved Photocatalytic Activity

There are many methods of fabricating ZnO nanostructured materials, including solution-based and vapour-phase methods. However, some of the challenges with most solution-based preparation procedures are: (i) reproducibility due to the constraint of using metal salts of variable purity, (ii) the slow rate of crystal growth, and (iii) the necessity of shaping agents for well-regulated morphologies. Most synthetic strategies for Vis/solar light-responsive semiconductors aim for a reduction in the band gap energy and the effective separation of the photogenerated (e^-/h^+) charge carriers. These two properties rely on the particle dimension of the semiconductor, its crystal phase, and degree of crystallinity, hence, the need for shaping agents [54] that produce increased specific surface areas for self-assembled nanoporous materials [55]. Controlling synthesis conditions ensures the fabrication of semiconductors with the desired photocatalytic properties. Some of the available methods for the solution-based synthesis of ZnO nanoparticles are sol-gel [56], chemical [57], precipitation [58], hydrothermal [59], microwave [60], and solvothermal [61] methods. It is important to highlight that the key advantage of the solution-based synthetic methods is their ease of implementation at a low cost with no need for sophisticated equipment. Mainly, reactions are conducted at ambient temperatures, hence, saving on energy costs. On the other hand, vapour-phase methods include thermal evaporation [62], pulsed laser deposition [63], physical vapour deposition [64], molecular beam epitaxy (MBE) [65], and others. The photocatalytic activity of ZnO nanoparticles is highly dependent on the starting materials and the fabrication conditions [66]. Many current preparation methods and reagents for controlling particle size and shape at the nanophase are still experimental bottlenecks. Nonetheless, some of the more promising current procedures for fabricating ZnO nanoparticles are discussed below.

2.1. Sol-Gel Method

The sol-gel procedure is the most important wet-chemical technique for fabricating ZnO nanoparticles. The procedure is simple, inexpensive, and produces materials of high homogeneity and purity. Some disadvantages include a long processing time, contraction

during processing (may cause cracks), and residual (hydroxyl and/or carbon) groups, which is important because the morphology of the catalytic surface significantly affects the photosensitivity of sol-gel-derived ZnO thin films [67,68]. Therefore, research has been ongoing to fine-tune the microstructure (size and morphology) [69], homogeneity [70], and optical response efficiency of ZnO semiconductors through these solution-based syntheses protocols. A good example is the reported link between the shape and size of the ZnO nanoparticles and the concentration of surface hydroxide (OH^-) ions [71,72]. Hence, semiconductor shape controllers and capping agents were routinely added to the recipe [73–75]. However, it must be noted that a high photocatalytic performance has also been reported in the sol-gel synthesis of ZnO without a capping agent [69]. Similarly, high-temperature treatments are beneficial for the attainment of high crystallinity (minimum bulk defects), thereby favouring photocatalytic performance.

In the sol-gel method, metal alkoxide precursors undergo hydrolysis to form a colloidal suspension (sol). When the solvent is removed, a very porous and lightweight material called aerogel is produced (Equations (1)–(4)).

$$Zn^{2+} + 2OH^- \rightarrow Zn(OH)_2 \quad (1)$$

$$Zn(OH)_2 \rightarrow ZnO + H_2O \quad (2)$$

$$Zn(OH)_2 + 2OH^- \rightarrow [Zn(OH)_4]^{2-} \quad (3)$$

$$[Zn(OH)_4]^{2-} \rightarrow ZnO + H_2O + 2OH^- \quad (4)$$

Kalisamy et al. [76] have described the fabrication of a ZnO-embedded S-doped graphitic carbon nitride (g-C_3N_4) heterojunction nanocarbon material with a good reduction of charge carrier recombination and high photocatalytic breakdown of dyes that was achieved via a mediator-free Z-scheme mechanism. Only 50 mg of the material was required to completely remove the 10 ppm initial concentration of dye pollutants [76]. Shemeena et al. [77] prepared similar ZnO/g-C_3N_4 material utilising the sol-gel technique. Here, the g-C_3N_4 was prepared using melamine, and the ZnO/g-C_3N_4 material was prepared by adding a few grams of the g-C_3N_4 to a ZnO sol and then the suspension was stirred, dried, and treated at 300 °C. This synthetic strategy resulted in a reduced band gap, offsetting the drawbacks of pristine ZnO. Thus, the ZnO/g-C_3N_4 catalyst achieved 100% degradation of Congo red (10 ppm) in 120 min.

In addition, Wu et al. [78] described the sol-gel preparation of a ternary ZnO/Fe_3O_4/g-C_3N_4 composite material that photodegraded three different dyes. In preparing the composite, a few grams of ZnO/Fe_2O_3 and melamine with a mass ratio of 1:1 were pulverised and then dispersed in deionised water under sonication. The dried materials were annealed at 550 °C. The ternary magnetic composite material was recyclable and the photocatalytic performance was attributed to a redshift in its absorption edge. Similarly, a heterojunction of $AgIO_4$/ZnO with efficiently separated photoinduced charges was prepared following the sol-gel approach. The materials were obtained by mixing known volumes of a $AgNO_3$ solution with a prepared ZnO suspension. Then, a known amount of a $NaIO_3$ solution was added in drops with strong stirring and the suspension was filtered and dried. The photoreactivity of the $AgIO_4$/ZnO in the removal of the dyes was three times better than the pristine ZnO with 100 mg of the catalyst removing 98% of indigo carmine and 81% of rhodamine B dyes [79].

In addition, the overall photocatalytic performance of the ZnO semiconductor was improved when some carbon-based material, such as reduced graphene oxide (rGO) [80], carbon nanotube [81], or graphene oxide (GO), was utilised [77]. In this regard, Zhu et al. [56] prepared an Fe-Cu-ZnO/GO composite that exhibited good adsorption and photodegradation of dyes. The authors used the sol-gel technique to combine Fe and Cu with ZnO in a heterostructured material in which $C_{18}H_{29}NaO_3S$ was used as a shaping agent to control crystal growth. Graphene oxide was used to produce the gel that was dried

and treated at 400 °C to produce the Fe-Cu-ZnO/GO composite. The composite removed 99% of dark green dyes from contaminated water in 90 min.

2.2. Chemical Precipitation/Co-Precipitation

The method involves reacting precursor components in an appropriate solvent with a dopant added before precipitation occurs. Chemical methods involve precipitation from inorganic or organic solutions with an easy control of the nucleation, growth, and ageing of the solution. Its advantages include the easy control of particle size, composition, simplicity, and low-temperature processing, which may not involve an organic solvent. Some disadvantages of co-precipitation include:

- Impurities that may precipitate with the product;
- Time-consuming processes;
- Not applicable to uncharged species;
- Lack of batch-to-batch reproducibility;
- The difficulty encountered with handling components that precipitate at different rates.

Due to these shortcomings, the chemical precipitation method has been combined with other methods. Oppong et al. [75] have used the co-precipitation technique to prepare Vis active La-doped ZnO/GO nanostructured materials. In this synthetic approach, the La-doped ZnO was decorated on graphene oxide sheets to produce an advanced photocatalyst that overcame all the inherent deficiencies of unmodified ZnO. The material owes its efficient photocatalytic performance to doping with the lanthanum up to an optimally determined concentration, as higher amounts increased the recombination rate of the photoinduced charge carriers. Most importantly, the graphene oxide acted as an adsorbent for the eosin yellow dye, an enhancer of electron transfer, and an extender of visible light absorption. The study identified $^{\bullet}OH$ and $O_2^{-\bullet}$ as the radicals responsible for the photodegradation of the dye. TOC analysis further confirmed the complete mineralisation of the dye. The degradation was 3.2 and 4.5 times slower in the presence of 2-propanol and benzoquinone (as radical scavengers), respectively. Within 210 min, the catalyst removed 100% of 20 ppm of the dye in water [75].

Praveen et al. [82] used the sol-gel method to synthesise ZnO nanoparticles decorated with Ag nanoparticles to remove toxic methylene blue and Cr(VI) from aqueous solutions. The ZnO-Ag composites were prepared by the addition of a few grams of ZnO to an N^1[3-(trimethoxysilyl)propyl]diethylenetriamine (TPDT) solution containing $AgNO_3$, with the resultant solution then reduced and stirred strongly at room temperature. All the materials with varying concentrations of the TPDT/ZnO-Ag showed a redshifted Vis absorption edge, implying that the interaction of the TPDT matrix and Ag nanoparticles with ZnO shifted the band gap of the ZnO into the visible light region. Hence, 20 mg of the catalyst completely removed 1.5×10^{-5} M aqueous solution of the dye pollutant in 60 min. In another work aimed at circumventing some of the problems inherent in the synthetic methods presented thus far, metal complexes were used to produce innovative hybrid materials via controlled morphology growth and band-gap expansion. There was no need for a stabiliser to direct growth. Hence, Sarmah et al. produced a zinc-sodium acetate complex ($C_{32}H_{48}O_{34}Na_8Zn_4$) from a combination of zinc ($ZnC_4H_6O_4$) and sodium ($C_2H_3NaO_2$) acetates in a 1:2 molar ratio in methanol at ambient temperatures. Hydrolysis reactions with hydrazine hydrate in methanol under hydrothermal conditions at 150 °C were done to produce metal hybrid materials (S-1, S-2, and S-3) as hybrids with Cu, Ag, and Au, respectively [83]. In addition to FT-IR spectral analysis, the AAS data confirmed the success of the metal exchange reactions, and the Zn^{II}, $Cu^{0,}$ and Ag^0 were confirmed in samples of S-1 and S-2 from X-ray photoelectron spectroscopic (XPS) analysis. Under Vis irradiation, 20 mg of the prepared photocatalysts completely degraded 100 ppm concentration of various organic pollutants through H_2O_2 generation from H_2O and O_2.

2.3. Chemical Precipitation/Co-Precipitation Incorporating Other Techniques

Researchers occasionally incorporate other techniques into chemical precipitation. Zarrabi et al. [84] prepared ZnO/GO by precipitation using sonication. When ultrasound is applied to a solution, it causes simultaneous compression and expansion, creating cavities in the liquid [85]. However, the calcination process (>400 °C) removes the cavities, affecting particle dispersion, homogeneity, and morphology. The group indicated that using ultrasound in the synthetic process improved the performance of the photocatalyst. Improvements include a higher surface area, larger pore volume, narrow and uniform particle size distribution, and better Vis sensitivity; all of which enhanced catalyst performance and the successful removal of dye pollutants by degradation [84].

A mixed metal oxide (ZnO/MgO, 0.5 M/0.5 M) nanomaterial prepared by co-precipitation achieved good photocatalysis under Vis irradiation with good antibacterial properties for the degradation of wastewater from textile dyeing. A hierarchical CuO/ZnO p-n heterojunction nanomaterial (p-CuO and n-ZnO) synthesised by Bharathi et al. [86] facilitated the efficient transfer of electrons from one semiconductor to the other despite the lattice mismatch and small chemical interaction. The study reported that the CuO/ZnO materials degraded methylene blue under Vis irradiation. Similarly, Santos et al. [87] used a combination of chemical and co-precipitation techniques to prepare heterostructured Ag/ZnO nanomaterials for the degradation of methylene blue and reactive black 5 textile dyes. Other studies in which co-precipitation methods were used to achieve ZnO Vis active catalysts for dye degradation are listed in Table 3.

Table 3. Catalysts prepared by co-precipitation.

Precursor	Reaction Conditions	Morphology of Product(s)	Composite Photocatalyst/ Dosage	Catalytic Application	Catalytic Activity	Enhancements	Ref.
Zinc acetate dehydrate, cadmium chloride monohydrate and sodium sulphide nonahydrate	Precipitation and calcination	Platelets-like hexagonal wurtzite ZnO, hexagonal CdS and cubic CdO phases.	ZnO–CdS–CdO (50 mg)	Methylene blue and rhodamine B (2×10^{-5} M)	95% in 120 min.	Reduced band gap, improved. photocatalytic efficiency.	[58]
Zinc nitrate hexahydrate, copper(II) nitate trihydrate	Co-precipitation	Flake like shaped wurtzite Cu/ZnO.	Cu/ZnO/Dopant (500 mg/L)	Methylene blue (0.015 M)	4.7 times better than ZnO under solar irradiation.	Reduced charge carrier Recombination.	[88]
Zinc acetate dehydrate, urea and graphite flakes	Precipitation/wet chemical	Hexagonal wurtzite structure of N-ZnO densely packed on the surface of GO nanosheets	N-doped ZnO/GO (50 mg)	Brilliant green (20 ppm)	100% in 90 min.	Reduced band gap & reduced charge recombination.	[89]
Zinc acetate di-hydrate and gadolinium(III) nitrate hexahydrate	Co-precipitation	Spherical shaped crystalline wurtzite Gd-ZnO	Gd-ZnO (25 mg)	Methylene blue (10 ppm)	93% in 90 min.	Reduced charge recombination.	[90]

2.4. Hydrothermal Methods

The hydrothermal procedure has become the method of choice in recent times. As a reaction procedure with a high control of the temperature and pressure conditions in an autoclave (pressurised steel vessel lined with/without Teflon), it allows for the careful control of the crystallite size and form. In addition, the nature of the thermal treatment and precursor solution used determines the strength of the interfacial adsorption, surface area, and morphology of the material [91,92].

Zhang et al. [93] fabricated a graphitic C_3N_4-ZnO@graphene aerogel (g-C_3N_4-ZnO@GA) nanomaterial by adding sonication to the hydrothermal method. Hence, a few grams of graphene oxide and zinc nitrate in deionised water was sonicated, and then a known amount of g-C_3N_4 was added to the suspension before hydrothermal treatment and final freeze-drying. The high catalytic performance was ascribed to its ability to suppress the recombination of photoinduced e^-/h^+ pairs due to their efficient transfer across the heterostructure. An amount of 5 mg of the hybrid catalyst with a high adsorption capacity and superior photocatalytic activity removed up to 83% of 20 ppm of organic pollutants in 150 min [93].

Similarly, Zhang et al. [94] successfully prepared a 'pompon-like' structured g-C_3N_4/ZnO composite photocatalyst using a two-step method. SEM analysis revealed that the heterojunction formed by the g-C_3N_4 nanosheets was wrapped (not 100%) around the spherical surface of ZnO. The prepared catalyst g-C_3N_4/ZnO successfully degraded rhodamine B dye.

The chemical composition of a material often determines its electronic properties. The coordination structure of ZnO may be altered by replacing (doping) some metallic Zn atoms with other atoms of choice in the structure. This changes its optical behaviour to improve its photocatalytic response and integrity. Gaurav et al. [95] prepared the Cu ion-doped ZnO material via the combination of zinc nitrate and copper acetate solutions in deionised water, with the pH adjusted before hydrothermal treatment. The study reported that the shift in the optical band gap energy (as low as 3.11 eV) to longer wavelengths is directly related to the concentration of Cu ions in the lattice of the Cu:Zn material.

Venugopal et al. [96] reported the fabrication of the ZnO-Ag_8S hybrid material using a three-step method that included spin coating, a hydrothermal method, and successive ionic layer adsorption reaction (SILAR). SILAR is a simple and cheap thin-film deposition method for the fabrication of composite materials. In this method, the substrate was spin-coated, subjected to hydrothermal treatment and, finally, SILAR. The substrate was then washed with water to remove any species that are loosely bound to the surface. The thin film efficiently degraded rhodamine B dye. The high efficiency resulted from the dual beneficial effects of the photocatalyst and the electric potential between the two semiconductors [96]. In addition, Karunakaran et al. [97] prepared nanodiscs with cubic $ZnFe_2O_4$ as the core and face-centred-cubic Ag-deposited hexagonal ZnO as the shell. The $ZnFe_2O_4$/Ag–ZnO composite exhibited surface plasmon resonance in the Vis region due to the silver ions. The nanodiscs were superparamagnetic, with the surface area, pore volume, and pore radius reported as 26.83 $m^2\ g^{-1}$, 0.082 $cm^3\ g^{-1}$, and 4.88 nm, respectively. The combined solution of $ZnFeO_4$ and polyethylene glycol was sonicated, then zinc nitrate and silver nitrate solutions were added, and the pH was adjusted before microwave treatment. The catalyst exhibited excellent photocatalytic performance [97]. In another study, carbon-doped zinc oxide (C-ZnO) was found to alter the photoresponse of ZnO to the Vis region by altering its band structure. It also improved the photocatalytic performance of the catalyst by reducing the recombination speed of photogenerated charges and photocorrosion. $BiVO_4$ is a catalyst operating in the visible region with a small band gap energy of 2.4 eV, which suffers from a high recombination speed of e^-/h^+ charges. A composite C-ZnO/$BiVO_4$ was prepared to improve the catalytic properties for the efficient degradation of methylene blue under Vis irradiation. The ZnO and C-ZnO were prepared from zinc acetate, sucrose (carbon source), and CTAB in deionised water and subjected to hydrothermal treatment, respectively. Then, the obtained precipitate was calcined. Whereas the $BiVO_4$ was prepared by the hydrothermal method from a bismuth nitrate solution and ammonium metavanadate in HNO_3 and CTAB, the C-ZnO/$BiVO_4$ composite was synthesised by vigorously mixing the as-synthesised $BiVO_4$ and the C-ZnO in deionised water. The suspension was ultrasonicated, centrifuged, and dried [98]. As a photocatalyst, 75 mg of the material removed 100% of 10 ppm of the methylene blue dye in 50 min.

Other ZnO nanostructures fabricated by the hydrothermal method or combined with other techniques are summarised in Table 4.

Table 4. ZnO nanostructures prepared by hydrothermal methods.

Fabrication Method	Composite Photocatalyst/Dosage	Catalytic Application	Catalytic Activity	Enhanced Factors	Ref.
Hydrothermal	$ZnO/CuBi_2O_4$ + potassium persulfate/100 mg	MO, RhB & CR ($(1.0 \times 10^{-5}$ M))	75% RhB in 210 min	Larger surface area, heterojunction formation.	[59]
Hydrothermal	Cu-ZnO (50 mg)	MO (0.02 mM)	99.50% in 150 min	Good charge transfer & reduced charge recombination.	[95]
Hydrothermal, UV-C photoreduction	ZnO-Pt (1×1 cm thin film)	MB (10 μM)	90 min	Reduced charge recombination.	[99]
Microwave-assisted hydrothermal	ZnO, CdO (10 mg)	Alizarin Red (10 ppm)	92% & 80% in 75 min	Surface & morphology.	[100]
Hydrothermal	Au-ZnO (60 mg)	MB (10 ppm)	100% in 75 min	Good charge transfer & reduced charge recombination.	[101]

2.5. Microwave Synthesis Methods

The microwave method applies high-frequency electromagnetic waves (900–2450 MHz). Microwave synthesis causes simultaneous nucleation and growth, provides even heat distribution, decreases overheating, and prevents an undesirable phase-contrast which is common with hydrothermal techniques. Microwave energy is used to synthesise numerous ZnO nanoparticles. High crystallinity (minimum bulk defects) results from high-temperature treatment in solid-state reactions. However, it can cause the agglomeration of smaller particles, and decrease the active surface area. In general, catalytic performance increases with an increasing active surface area and crystallinity; and enhancing these important features simultaneously is quite challenging [29]. Based on these and other parameters, Manjunatha et al. [102] applied the Taguchi strategic method for the analysis of variance (ANOVA) and Grey relation analysis to prepare ZnO nanoparticles using predicted best conditions. Under the various experimental conditions, the best photocatalyst with a maximum degradation efficiency of the pollutant was identified. The research reported that: (1) a trivalent metal ion (Al^{3+}, Fe^{3+}, Cr^{3+})/ZnO nanocomposite material synthesised via the microwave-assisted solution combustion technique yielded the best catalyst, (2) crystallite size is mainly affected by the treatment temperature, and (3) with a contributing factor of 85.77%, the type of dopant had a primary influence on the band gap. The group reported that the best catalyst achieved an 89% removal rate of the methylene blue dye in 160 min. The combination produced a photocatalyst with a crystallite size of 46.96 nm and a band gap of 3.05 eV [102].

In another example of the microwave synthesis of a ZnO nanostructure, Saad et al. [103] reported the synthesis of a chitosan/ZnO and a chitosan/Ce–ZnO nanocomposite material. In synthesising the composite, zinc nitrate and chitosan in deionised water were stirred vigorously, with the pH adjusted to form a suspension that was microwaved. The chitosan/Ce–ZnO (doped with 1% cerium) was prepared by following a similar procedure with the addition of $Ce(NO_3)_3$ at the first step. The composites had reduced band gap energies and exhibited good stability and reusability up to the fifth cycle with minimal reduction in photocatalytic performance.

Vignesh et al. [60] investigated the antibacterial and photocatalytic effectiveness of a polyvinylpyrrolidone (PVP)-capped Cd/Ag/ZnO nanocomposite fabricated by the use of microwave-aided precipitation. Silver nitrate, cadmium nitrate, zinc nitrate, and a few grams of PVP were dissolved in ethanol and deionised water, then precipitated with NaOH and microwaved. The obtained material was then sonicated, dried, and subjected to a

high-temperature treatment. This synthetic approach prevented grain growth, but the lattice and cell parameters were slightly enhanced. When applied as a photocatalyst, the material completely degraded the methylene blue dye and showed good recyclability up to the fifth cycle with good stability.

2.6. Other Relevant Methods

Despite the wide variety of available nanoparticle synthesis methods, research has continued to evolve to produce catalysts with predefined properties through the combination and modification of existing ones and the development of novel routes. Other relevant methods for the fabrication of visible-light-driven ZnO photocatalysts are summarised in Table 5.

A highlight is the work by González-Casamachin et al. [104], who reported a ZnO on polypyrrole (PPy)-composite material synthesised by combining precipitation and polymerisation techniques. For the ZnO, solutions of $ZnCl_2$ and a surfactant in deionised water were mixed vigorously, precipitated using NaOH, and dried. While for the ZnO/Ppy, the ZnO nanoparticles, sodium dodecyl sulphate, and pyrrole in ammonium persulphate (for the polymerisation reaction) were thoroughly mixed. Methanol was then used to precipitate the ZnO/Ppy. The photocatalyst achieved a 66% TOC removal of the acid violet 7 pollutant dye in a continuous reactor system.

Table 5. Other methods of synthesis and applications of ZnO-based photocatalysts.

S/N	Fabrication Method	Catalyst/Type/Dosage	Catalytic Application	Catalytic Activity	Enhanced Factors	Ref.
1	Solvothermal	BiOCl/ZnO (50 mg)	RhB (10 ppm)	100% in 15 min	Charge separation by heterojunction.	[61]
2	Thermal oxidation, sulfidation & hydrothermal	CuO/CuS/ZnO (1 cm × 2 cm foam)	RhB (5 ppm)	93.20% in 160 min	p–n junction, reduced charge recombination.	[62]
3	Pulsed laser ablation/ Photodeposition	ZnO/Au/Pd (0.5 mg)	MB (5.0×10^{-5} M)	97% in 180 min	Synergistic effect between the ZnO, Au and Pd metals.	[63]
4	Fungal-secreted enzymes and proteins/sol-gel process	CuO/ZnO/binary oxide (40 mg)	MB (10 ppm)	97.00% in 85 min	Increased ratio of ZnO, increases particle size, improves efficiency.	[105]
5	Vegetable waste extracts as potential structure-directing agents	ZnO–CuO (25 mg)	MB (0.001 M)	95.60% in 120 min	Nanosization & p–n heterojunctions allowing better e^-/h^+ separation.	[106]
6	High-energy ball milling	Ni co-doped Al-ZnO (50 mg)	MO & CR (10 ppm)	100% MO in 30 min	Enhanced charge separation and visible light response.	[107]
7	Surfactant-assisted hydrothermal method	ZnO and g-C_3N_4 (1 g)	MB & RhB (10 ppm)	97% MB in 50 min	Enhanced charge separation and visible light response.	[108]
8	One-pot recrystallisation	ZnO–SWCNT (130 mg)	MB (7.9×10^{-4} M)	100% in 120 min	Chemical bonding promotes light absorption and reduced charge recombination.	[109]
9	Jet nebuliser spray pyrolysis	ZnO/g-C_3N_4/Ag/ thin film	MB & MG (1×10^{-5} M)	96% & 99% in 90 min	Reduced band gap & reduced charge recombination.	[110]
10	Solvent-free synthesis	ZnS-ZnO/graphene (10 mg)	MB & MO (1×10^{-5} M)	99% in 90 min & 97.5% in 160 min	Reduced band gap, good charge transfer & reduced charge recombination.	[111]
11	Parallel flow precipitation	Fe-ZnO (50 mg)	RhB (10 ppm)	84% in 120 min	Higher specific surface area & charge separation efficiency.	[112]
12	Low-temperature precipitation	Chl-Cu/ZnO (30 mg)	RhB (60 ppm)	99% in 120 min	The synergy between chlorophyll and Cu improved visible light response.	[113]

3. Characterisation Techniques and Structural Analysis

3.1. General Structure of ZnO

The bonds in a ZnO semiconductor are tetrahedrally bound, giving it similar electronic properties to diamond, zinc blende (cubic ZnS), wurtzite (hexagonal ZnS), and chalcopyrite ($CuFeS_2$) [41]. The electronic configuration of zinc blende and wurtzite are almost undistinguishable. Although this is typical of covalent sp^3-hybridised bonds, the bonds between the Zn^{2+} and O^{2-} contain a significant ionic component [44]. As shown in Figure 2, ZnO is a binary compound that primarily crystallises in a tetrahedrally coordinated wurtzite-type assembly sharing a crystal structure with rock salt (NaCl, B1), zinc blende (B3), and wurtzite (B4).

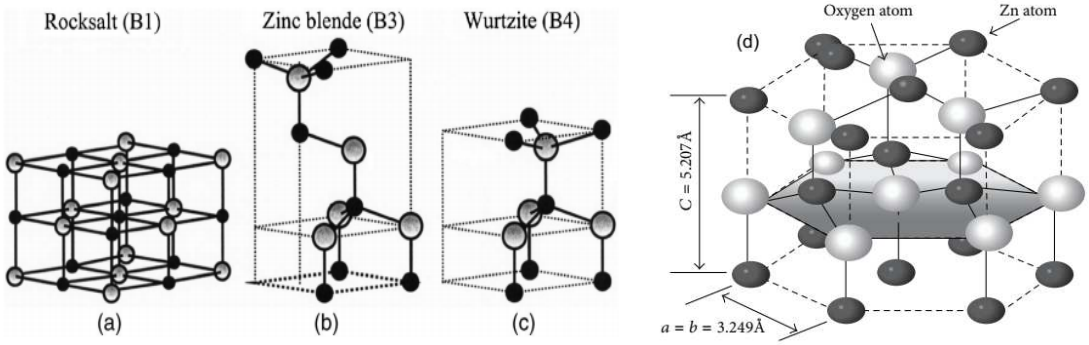

Figure 2. Structures shared by ZnO: (**a**) rock salt, B1; (**b**) zinc blende, B3; and (**c**) wurtzite, B4 (**d**) tetrahedral ZnO. The shaded grey and black balls represent O and Zn atoms, respectively [114].

3.2. Classification of ZnO Nanostructures

The structure and properties of ZnO nanoparticles determine their field of application. Many previous studies have attempted to produce ZnO with various nanostructures [115]. Zero-dimensional (0D), one-dimensional (1D), two-dimensional (2D), and three-dimensional (3D) nanostructured representations of ZnO have been published, as shown in Figure 3, with (field effect)-scanning electron microscopy (FE-SEM and SEM) illustrations.

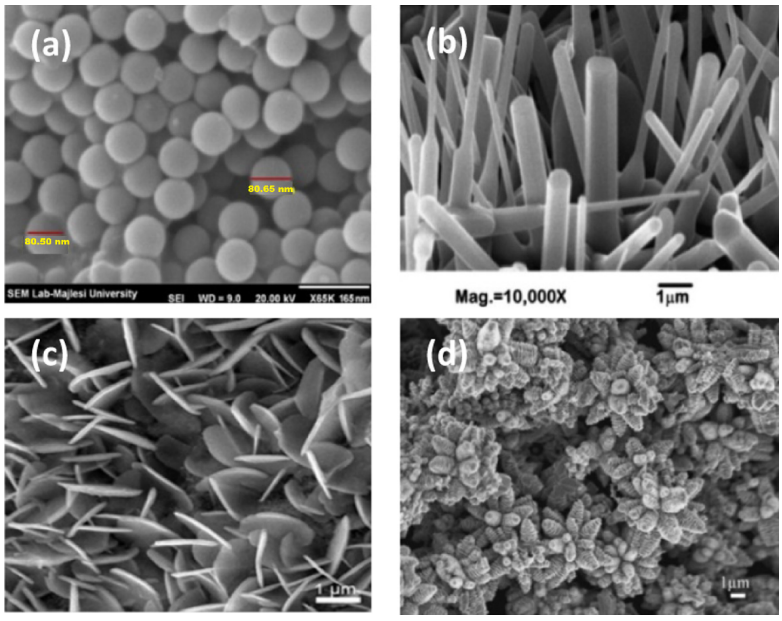

Figure 3. Microscopic images of zinc oxide (FE-SEM and SEM) represented in (**a**) 0D, (**b**) 1D, (**c**) 2D, (**d**) 3D [53].

Nanoparticles have large surface areas and are standard in visible light photocatalysis because more active sites are available where contaminants can be readily adsorbed. Surprisingly, nanowires with lower crystallinity and more defects have been shown to have an advantage in photocatalytic applications. This may result from the hydroxyl groups bound to the defects facilitating the trapping of photoinduced (e^-/h^+) pairs and improving their separation, thereby increasing activity.

3.3. Electronic Structure of ZnO

ZnO exhibits a large band gap with a tendency for n-type conductivity similar to other binary transparent conductive oxides (In_2O_3, SnO_2, and CdO). The partly ionic nature of the bonds between the Zn^{2+} and O^{2-} ions accounts for the reasonably high electronic conductivity. The conduction band has an almost exclusive Zn^{2+} 4s orbital character, and the valence band is formed by the 2p orbital character of the O^{2-} ions [116]. Hence, hole mobility up to $\mu_p \approx 3\ cm^2\ V^{-1}\ s^{-1}$ has been registered for p-doped ZnO [41,117,118], while electron mobility in thin undoped films can exceed 5000 $cm^2\ V^{-1}\ s^{-1}$ at 100 K [119].

3.4. Structural Analysis and Characterisation

The structural characterisation of nanoparticles has been studied using many approaches to determine important parameters, including size, crystallinity, constituents, distribution, and other qualitative features. Physical characteristics can be assessed using many methods depending on the circumstances. Since each instrumental technique has a limit of sensitivity, selecting the best method is difficult, and a combination of characterisation techniques is frequently required. Furthermore, given the growing importance of nanoparticles in fundamental research and applications, researchers from many areas must work together to mitigate the difficulties of reproducibility, comparability, and reliability of characterisation data postsynthesis. Here, we present current knowledge on using various experimental methods to characterise ZnO nanoparticles. The characterisation techniques are categorised based on the concept/group of the method, the data they may give, or the type of nanoparticle for which they are intended. Some of the available analytical techniques and the type of analysis achieved are summarised in Table 6 and elaborated on in the following sections.

Raj et al. [57], Bharathi et al. [86], and Santos et al. [87] used characterisation techniques that include PXRD, Raman, SEM, TEM, HRTEM, and EDS to establish the identity of prepared zinc oxide composite materials. Some PXRD diffractograms are represented in Figure 4a,b.

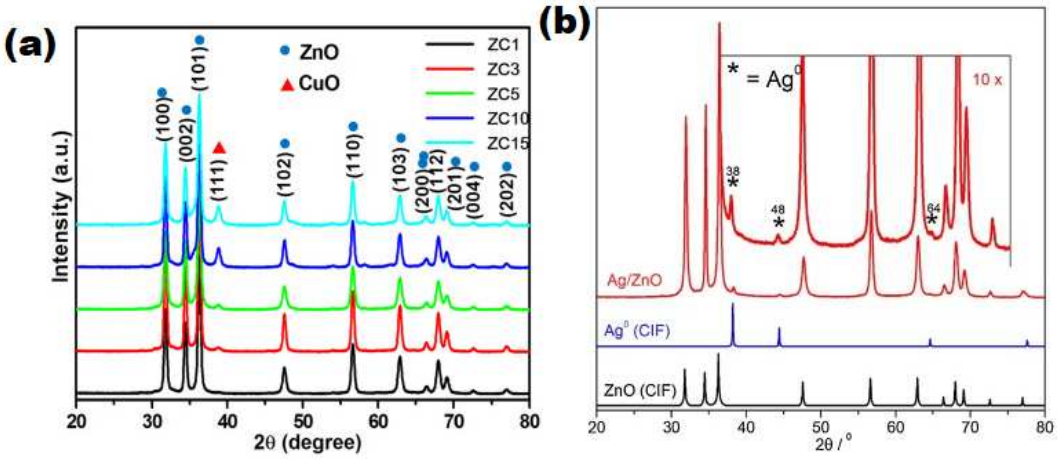

Figure 4. Representative PXRD of zinc oxide composite materials: (**a**) ZnO/CuO [86], (**b**) ZnO/Ag (* = peaks associated with Ag^0) [87].

Table 6. Summary of characterisation techniques [120].

Technique/Method	Parameters Determined
Powder XRD	Crystal structure, composition, crystallite size.
XAS (EXAFS, XANES)	X-ray absorption coefficient (element-specific)—oxidation state of species, inter-atomic distances.
XPS	Electronic structure, elemental constituents, chemical states, ligand binding (surface-chemistry).
SEM-HRSEM, T-SEM-EDX	Morphology, dispersion of nanoparticles in cells and other matrices/supports, oxidation state.
Electron backscatter diffraction	Crystal configuration, grain texture, defects, shapes, and distortion.
Atomic force microscopy	Morphology in 3D mode, nanoparticle morphology, and examination–elemental composition.
High-resolution TEM (HRTEM)	TEM information and the crystal structure of single particles. Study defects differentiate between monocrystalline, polycrystalline, and amorphous nanoparticles.
Electron diffraction	Crystal structure, lattice parameters, study order-disorder transformation.
EELS (EELS-STEM)	The qualitative oxidation state of atoms, chemical environment, bulk plasmon resonance.
Aberration-corrected (STEM, TEM)	Nanoparticle clusters, homogeneity and phase segregation.
Electron tomography	The actual 3D image down to the atomic scale.
Scanning TEM	Morphology, structure, elemental constituent and hetero-interfaces.
FTIR	Surface chemical state.
Low energy ion scattering	Thickness and chemical constituents of nanoparticles.
Secondary ion mass spectrometry	Chemical information (surface-chemistry), molecular coordination and configuration, surface structure.
Brunauer–Emmett–Teller	Surface area, pore size.
Liquid TEM	Study growth mechanism (in real-time), single particle motion, and superlattice formation.
ICP-MS	Elemental constituents and nanoparticle concentration.
Ferromagnetic resonance	Nanoparticle size, homogeneity, shape, crystallographic defects, surface constituents, M values, magnetic anisotropic constant.
Transmission electron microscopy (TEM)	Nanoparticle shape and aggregation state.
Thermogravimetric analysis	Thermal stability.
UV-Vis	Absorption characteristics and hints on nanoparticle shape.
Photoluminescence spectroscopy	Optical profile– relation to crystal structural properties and constituents.
Dynamic light scattering	Detection of aggregation.
Nanoparticle tracking analysis and Differential scanning calorimetry	nanoparticle size and homogeneity.

Abbreviations: EELS—Electron energy loss spectroscopy; FTIR—Fourier transform infrared spectroscopy; ICP-MS—Inductively coupled plasma mass spectrometry; SEM-HRSEM-EDX—Scanning electron microscopy- high-resolution scanning electron microscopy-energy dispersive X-Ray analysis; UV—Ultraviolet; VIS—Visible light; XAS (XANES, EXAFS)—X-ray absorption spectroscopy (X-ray absorption near edge structure, extended X-ray absorption fine structure); XPS—X-ray photoelectron spectroscopy; XRD—X-ray diffraction.

The PXRD diffraction patterns presented in Figure 4a displays the PXRD patterns of a series of CuO/ZnO composite materials denoted ZC1-15 depending on the relative weight percentage of Cu to Zn in each material [**ZC1** = CuO/ZnO with 1% weight, **ZC3** = CuO/ZnO with 3% weight, **ZC15** = CuO/ZnO with 15% weight]. It is important to note that CuO is monoclinic (JCPDS 05-0661), and the ZnO is in a hexagonal phase (JCPDS 05-0664). The ZnO peak steadily decreased as the Cu/Zn weight percent increased (3–15 wt%). Due to the low percentage weight of CuO in composite **ZC1**, only ZnO peaks were observed. In contrast, samples **ZC3** to **ZC15** showed CuO diffraction peaks at

2θ = 38.75°, which match the (111) plane of the monoclinic crystal system. Figure 4b represents the PXRD pattern of a Ag-doped ZnO material that is matched to the diffraction peaks from the crystallographic information file (CIF CODE = 9,004,178) for the wurtzite structures of ZnO. Most of the observed peaks in the Ag/ZnO composite are related to the wurtzite structure of ZnO with the low-intensity peaks at 38°, 44°, and 64° accounting for the metallic silver with an fcc-structure (CIF CODE = 9,012,961).

Various techniques are used to analyse a material's surface chemistry, including EDS, XAS (EXAFS, XANES), low-energy ion scattering, and others (see footnote of Table 6 for abbreviations). However, X-ray photoelectron spectroscopy is often used to correctly identify the elemental composition of composite materials, which is often required when highly specific catalysts or materials are targeted. In order to confirm metal exchange, Sarmah et al. [86] analysed their synthesised composite materials using XPS as shown in Figure 5. ZnO, $Cu^{0,}$ and Ag^0 were confirmed in the samples from the XPS spectral analysis. The spectra showed two peaks in the 1016–1044 eV region for Zn $2p_{3/2}$ and Zn $2p_{1/2}$ with Δm ~ 23 eV, which confirmed the presence of ZnO in the samples. The absence of a satellite peak at 940 and 945 eV in the HR-XPS spectra confirmed the absence of copper oxide (Cu_2O and CuO) in the synthesised materials.

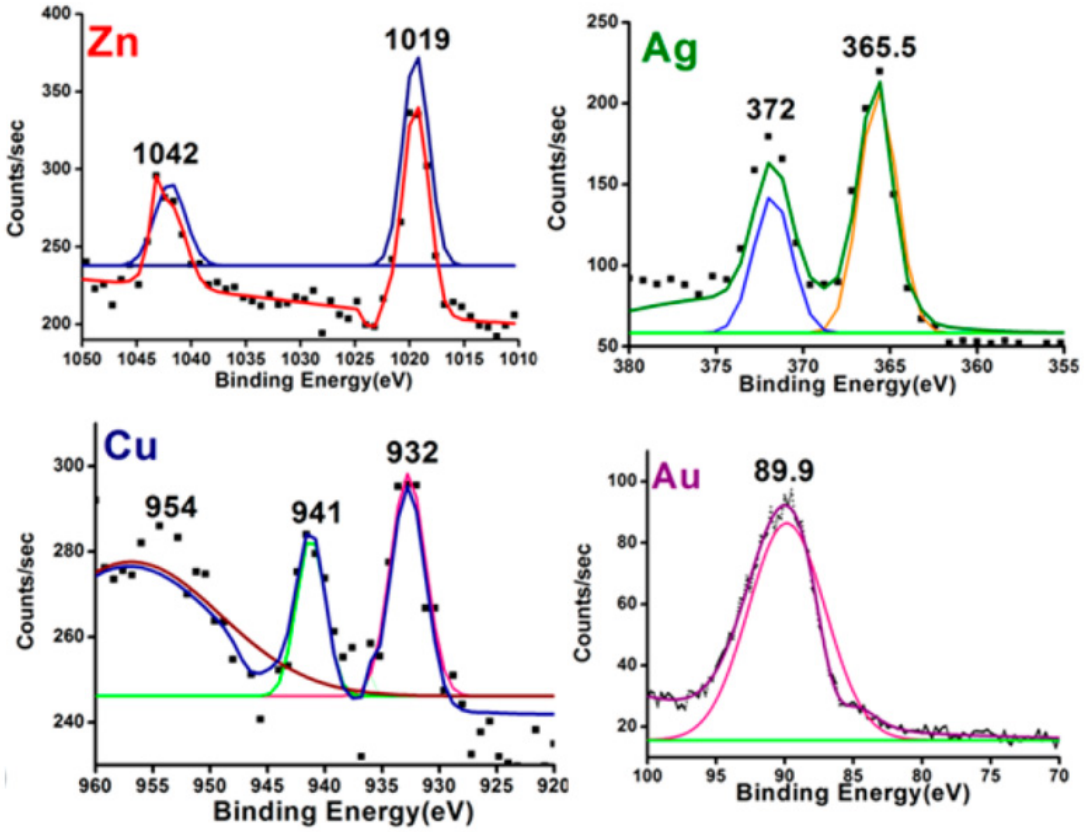

Figure 5. HR-XPS spectra of prepared ZnO nanocomposite materials. Red = zinc; green = silver; blue = copper; pink = gold; black squares = data points [83].

Karunakaran et al. [97] characterised their superparamagnetic $ZnFe_2O_4$-core/Ag on ZnO shell nanodisks using SEM, EDX, HRTEM, and selected area diffraction (SAED) analysis. In their report, the SEM analysis revealed the morphology of the synthesised material. In addition, EDX and SAED revealed the unit cells as cubic for $ZnFe_2O_4$, hexagonal for ZnO, and face-centred-cubic for Ag. The HRTEM image revealed a core/shell structure with a homogeneous and constant whitish-grey covering over a blackish-grey surface. Since iron has a blackish hue, the blackish-grey core is attributed to $ZnFe_2O_4$, while ZnO is responsible for the white-grey shell.

The EDX of the synthesised material revealed the presence of the constituent elements zinc, iron, silver, and oxygen. In addition, the absence of other elements confirmed the purity of the material. The electron diffraction spots in the synthesised sample validate the presence of hexagonal ZnO, cubic $ZnFe_2O_4$, and cubic metallic silver in the sample. Reflection spots were observed at 220, 422, 440, 551, 553, 622, 511, and 800 planes for the cubic $ZnFe_2O_4$; 100, 002, 110, 104, 203, and 211 planes for the hexagonal ZnO and 200 plane for the cubic Ag. The references for cubic $ZnFe_2O_4$, hexagonal ZnO, and cubic Ag are JCPDS card nos. 22-1012, 36-1451, and 04-0783, respectively.

Similarly, for the PVP-capped Cd/Ag/ZnO heterocomposites fabricated by the use of microwave-aided precipitation by Vignesh et al. [60], they reported PXRD diffraction patterns (Figure 6) with diffraction peaks at 2θ angles of 31.62°, 34.30°, and 36.04° allocated to the typical ZnO planes (JCPDS: 36-1451), indexed as the hexagonal wurtzite structure. While other PXRD planes are assigned to the typical CdO (111), (200), and (220) (JCPDS: 05-0640), and for AgO, the planes are (200) and (220), which matched with (JCPDS: 741743). The PXRD analysis indicated a decrease in crystallinity after doping with the different metals. It also shows that the crystallite size ranges vary with the calcination temperature, such that a range of ~79–41 nm was obtained for the samples calcined at 450 °C, while the sizes decreased dramatically (68–29 nm) for samples calcined at higher than 600 °C.

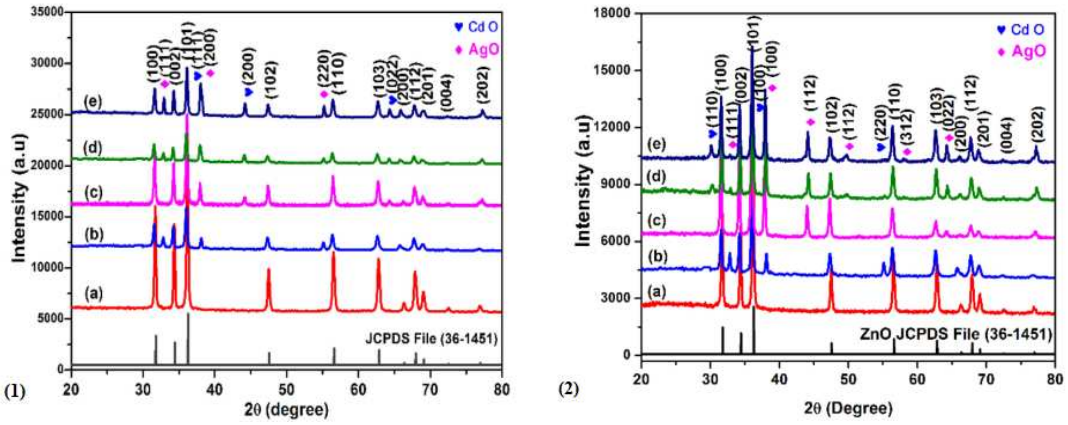

Figure 6. PXRD patterns of as-prepared ZnO (a), Ag:ZnO (b), Cd:ZnO (c), Cd:Ag:ZnO (d), and Cd:Ag:ZnO:PVP (e) materials [60]. Temp = 450 °C (**1**) and 600 °C (**2**).

Hence, the activity of the as-prepared Cd:Ag:ZnO:PVP heterostructured material was 4.7 times higher than the undoped ZnO. They also reported that 30 mg of the material degraded 99% of 20 mg/L of the methylene blue dye within 120 min of Vis irradiation [63].

In another study by Shanmugan et al., the authors investigated the link between the structural, optical, and photocatalytic properties of the bi-metallic (Sn and Cu)-doped ZnO nanoparticles. The Sn:Cu/ZnO nanocomposite was prepared using the microwave-assisted ultrasonication-precipitation method [121].

As shown in Figure 7, the EDX analysis established the extent of the Cu and Sn doping (atomic %) in the Zn matrix, which improved the light absorption intensity in the Vis region.

The XPS data of the Sn:Cu/ZnO composite material are presented in Figure 8. The data allow for the identification of the binding energy, electronic nature, charges on each element, and the functional groups of the nanomaterial. The data revealed peaks that match Zn (2p), O (1s), Sn (3d), and Cu (2p) for all the doped nanomaterials (Figure 8a). The addition of Cu^{2+} ions caused Sn^{4+} ions to be displaced with a higher energy than normally observed for the ZnO framework. In addition, when zoomed in, the data revealed that the Zn (2p) signal was split into two symmetrical peaks (Figure 8b). The Zn ($2p_{3/2}$) and Zn ($2p_{1/2}$) were observed at 1022 eV and 1045.2 eV, authenticating the spin-orbit coupling of the Zn^{2+} ion.

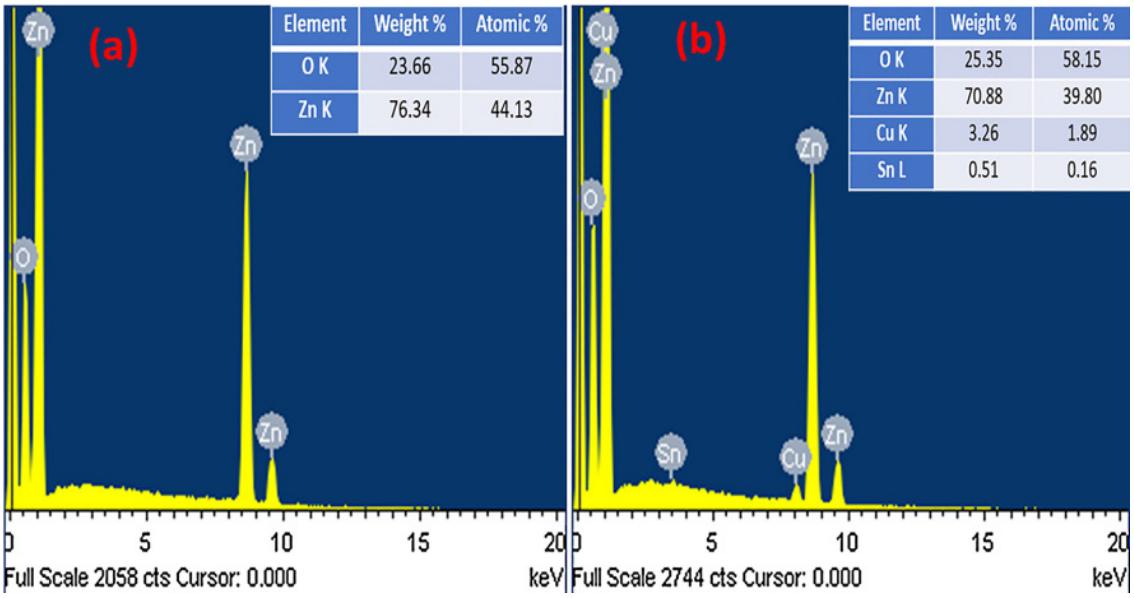

Figure 7. EDX spectra of ZnO (**a**) and Sn:Cu/ZnO (**b**) nanoparticles [121].

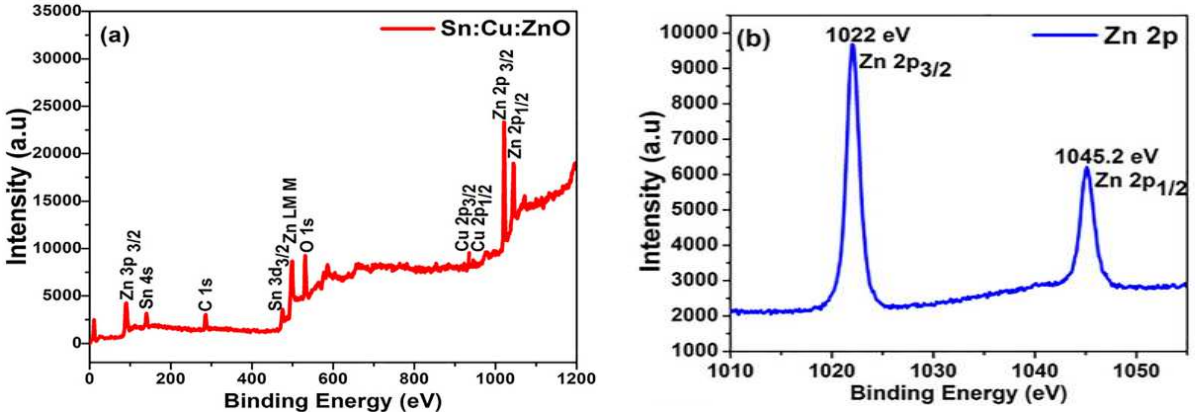

Figure 8. XPS data of the Sn:Cu/ZnO nanomaterial [121].

Many researchers have also used advanced analytical techniques to confirm the formation/creation of new materials by the use of imaging techniques, monitoring the changes in surface composition and structural defects. For example, Kalisamy et al. [76] described the preparation of a ZnO-implanted S-doped g-C_3N_4 heterojunction with a reduced recombination of photoinduced charges and improved catalytic breakdown of dyes. The TEM analysis of the composite material (Figure 9a) confirmed the deposition of ZnO nanoparticles on the S-doped g-C_3N_4 nanosheets, and the HRTEM reported inter-planar separations of 0.28 nm (110) and 0.24 nm (101) (Figure 9b).

In addition, Zhang et al. [93] prepared a g-C_3N_4-ZnO@graphene aerogel (g-C_3N_4-ZnO@GA). The microstructure (SEM image) of the g-C_3N_4-ZnO@GA (30%) presented in Figure 10a,b revealed the 3D porous structure of the graphene aerogel. Furthermore, the HRTEM images, Figure 10c,d, confirmed the formation of the heterojunction by the analysis of the lattice fringes at 0.280 nm and 0.326 nm, consistent with the (002) and (100) planes of ZnO and g-C_3N_4, respectively, which established their co-existence in the heterojunction.

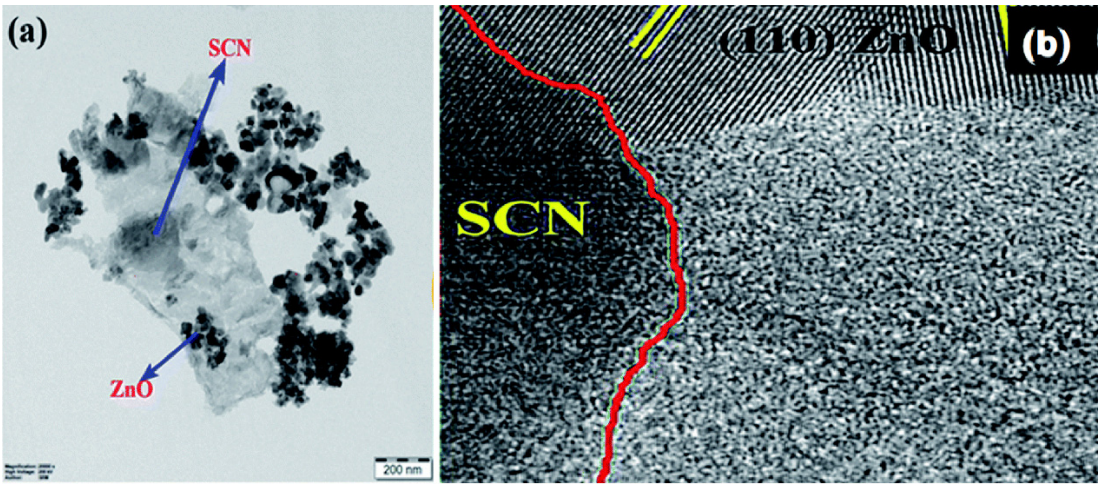

Figure 9. Images of ZnO/S-doped g-C_3N_4 material (**a**) TEM, (**b**) HRTEM [76].

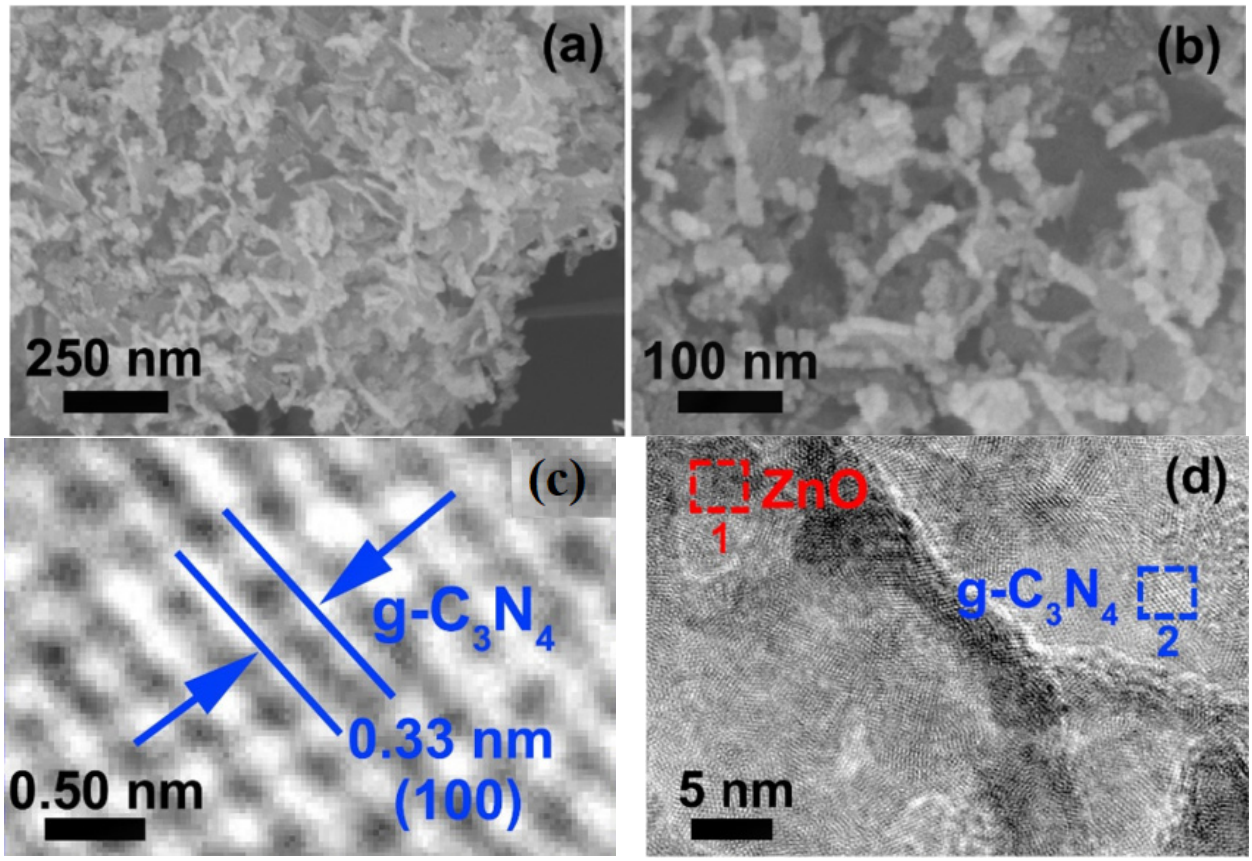

Figure 10. SEM (**a**,**b**) and HRTEM images (**c**,**d**) of g-C_3N_4-ZnO@GA (30%) [93].

Similarly, Zhang et al. [94] successfully prepared a g-C_3N_4/ZnO composite photocatalyst using a two-step method. The heterojunction structure comprises flakes of g-C_3N_4 coated on the ZnO surface with a width of 2.5 µm. Analysis of the SEM image revealed that the heterojunction formed by the g-C_3N_4 nanosheets was not completely wrapped around the spherical surface of the ZnO. This contrasts with the 3D heterostructure of g-C_3N_4-ZnO@GA (Figure 10).

Oppong et al. [75] used FTIR analysis to study the synthesised ZnO and ZnO-GO nanocarbon material and reported the identity of key functional groups in the materials, as

shown in Figure 11. These include the C-OH, C=C, and C=O stretch at low wavenumbers and the absorption of the surface OH groups identified at circa 3700 cm^{-1}.

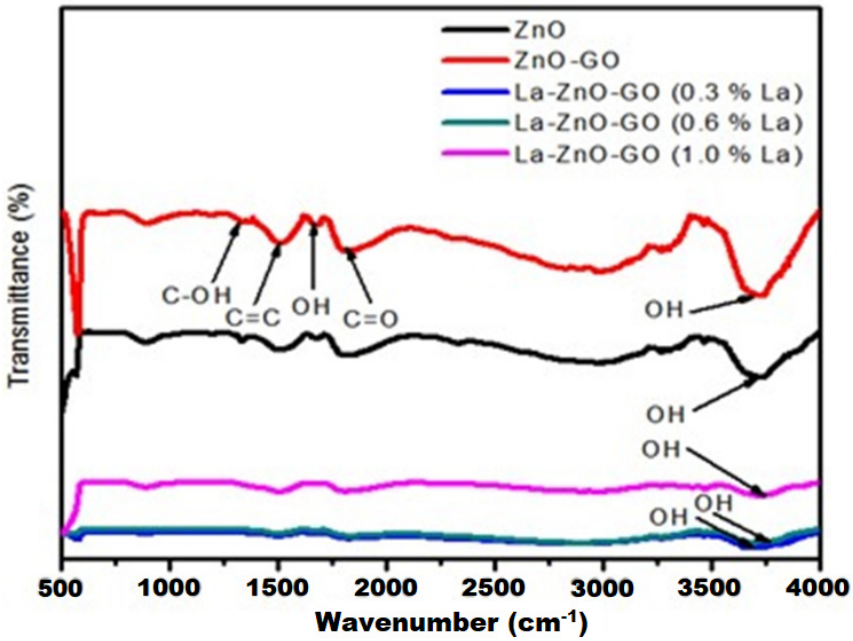

Figure 11. FT-IR spectra of La-doped-ZnO nanomaterials decorated on graphene oxide [75].

Furthermore, Raman analysis of the ZnO, ZnO/GO, and 0.3% La/ZnO/GO revealed the presence of strong peaks of ZnO at 331, 442, and 589 $cm^{-1,}$ which arose due to defects in the ZnO/GO via oxygen vacancy as shown by the D band defects observed around 1350 cm^{-1} in Figure 12. The optical response of the ZnO changed due to its modification with La and graphene oxide (Figure 12a).). In addition, the G bands originate from the in-plane tangential stretching of the carbon–carbon bonds in the graphene structure (Figure 12b Compared to pure ZnO, the combined impact of the graphene oxide and La improved the Vis absorption. This strategic doping with La/GO decreased the band-gap energy level due to the modification of the ZnO conduction band, resulting in the Vis absorption. Apart from being a sensitiser (absorbing Vis), graphene oxide acted as an electron collector by creating a new energy level in the band gap, allowing photoinduced electrons from this energy level into the conduction band of ZnO. The ultra-violet-diffuse reflectance (UV-DRS spectra are shown in Figure 13a, while the band gap of the materials was estimated using the Kubelka–Munk function ($F(R)$), presented in Figure 13b.

Srinivasan et al. [98] reported on the influence of carbon doping and modification with $BiVO_4$ on the properties of ZnO nanomaterials. The optical profile of the synthesised materials was studied by ultra-violet-diffuse reflectance (UV-DRS) and photoluminescence (PL) spectroscopies. They reported that the absorption band gap edge of C-ZnO had shifted to 412 nm (due to the embedded carbon) compared to the absorption edge of pure ZnO recorded at 396 nm, (Figure 14a,b).

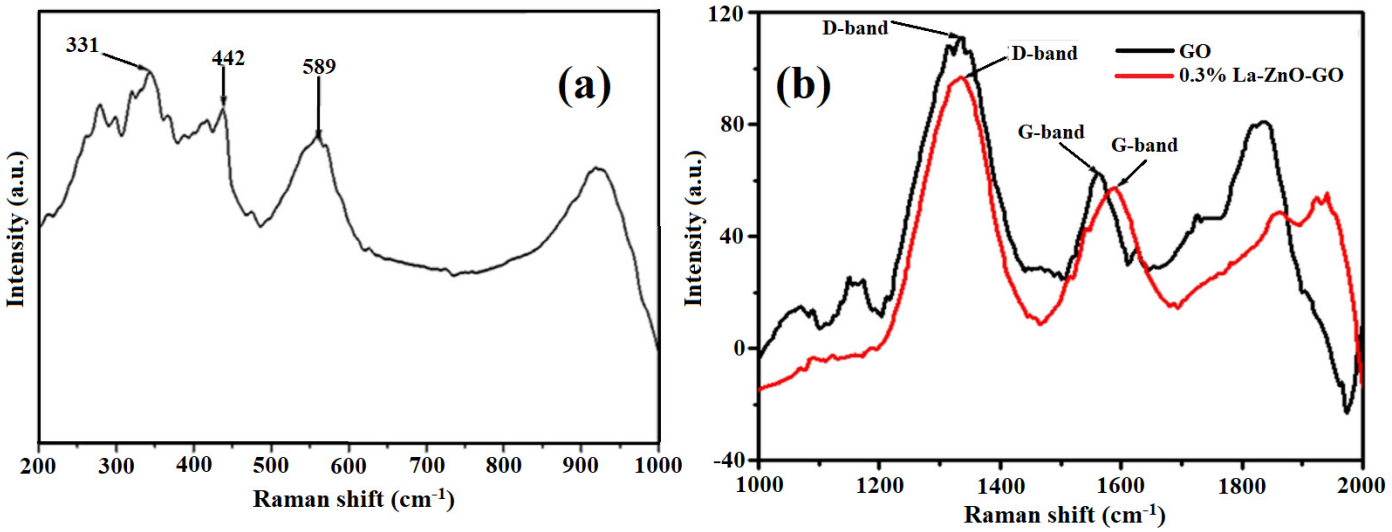

Figure 12. Raman spectra of (**a**) zinc oxide and (**b**) graphene oxide and 0.3% lanthanum-doped zinc oxide-graphene oxide [75].

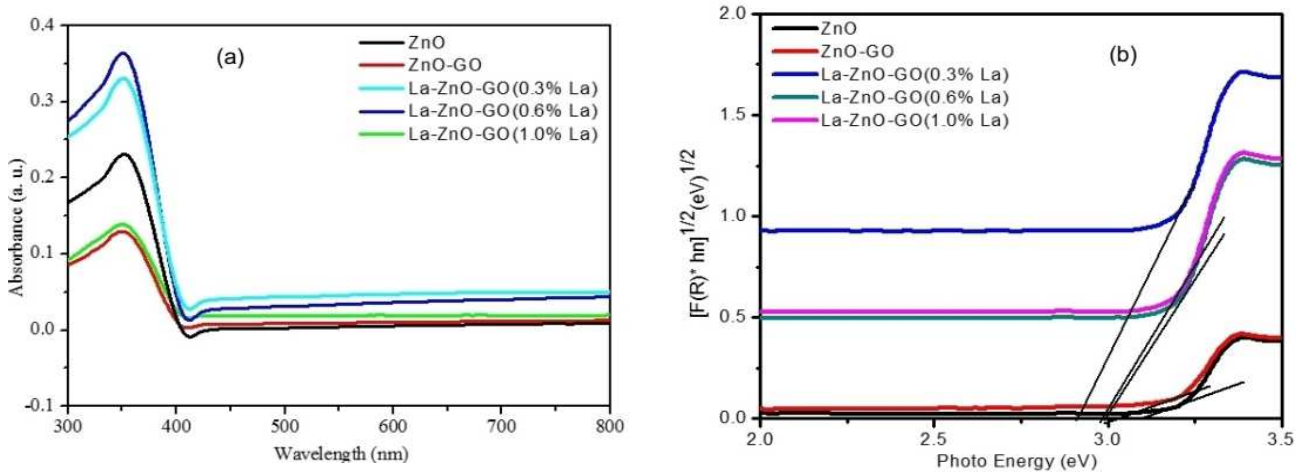

Figure 13. UV-Vis spectra (**a**) and Tauc plots (**b**) for La-doped-ZnO nanomaterials decorated on graphene oxide [75].

Furthermore, at 427 nm and 540 nm, two absorption edges belonging to C-ZnO and $BiVO_4$ (Figure 14c) displayed a wider absorption in the visible section for the C-ZnO/$BiVO_4$ material represented in Figure 15d. At the same time, PL spectroscopy also revealed a near band-edge emission peak for ZnO, C-ZnO, and C-ZnO/$BiVO_4$ at 389.56, 390.33, and 393.19 nm, respectively. The spectral (Figure 15e) investigation corroborated the reduction in the band gap energy of the samples of C-ZnO and C-ZnO/$BiVO_4$. Compared to pure ZnO, the decrease is due to carbon incorporation into the ZnO and composite formation between C-ZnO and $BiVO_4$. The suppression of the PL peak intensity demonstrated the effective separation of photoinduced charges in the C-ZnO and C-ZnO/$BiVO_4$ nanomaterials.

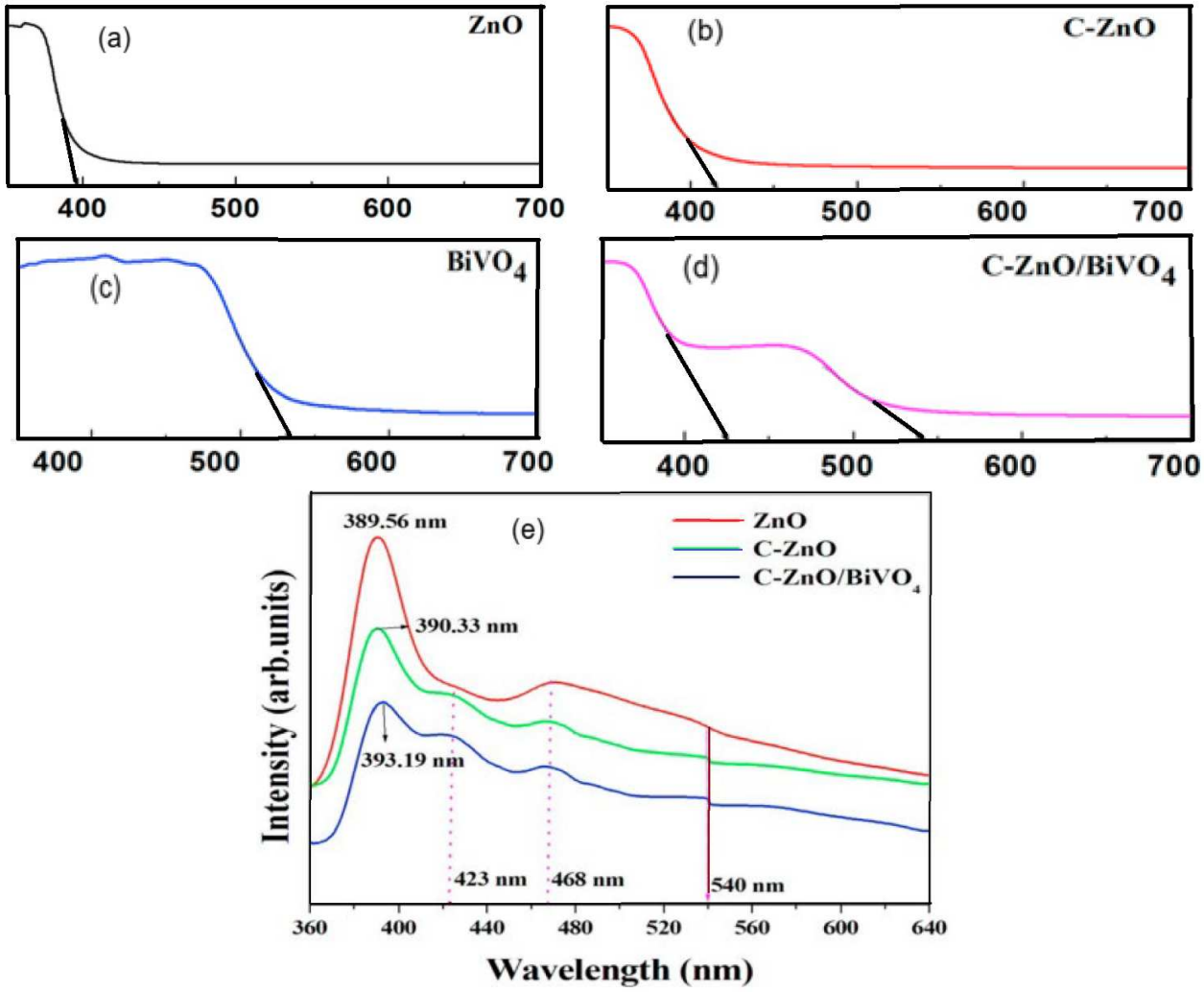

Figure 14. UV-DRS (**a**–**d**) and PL spectral data (**e**) of C-doped ZnO nanomaterials coupled with $BiVO_4$ [98].

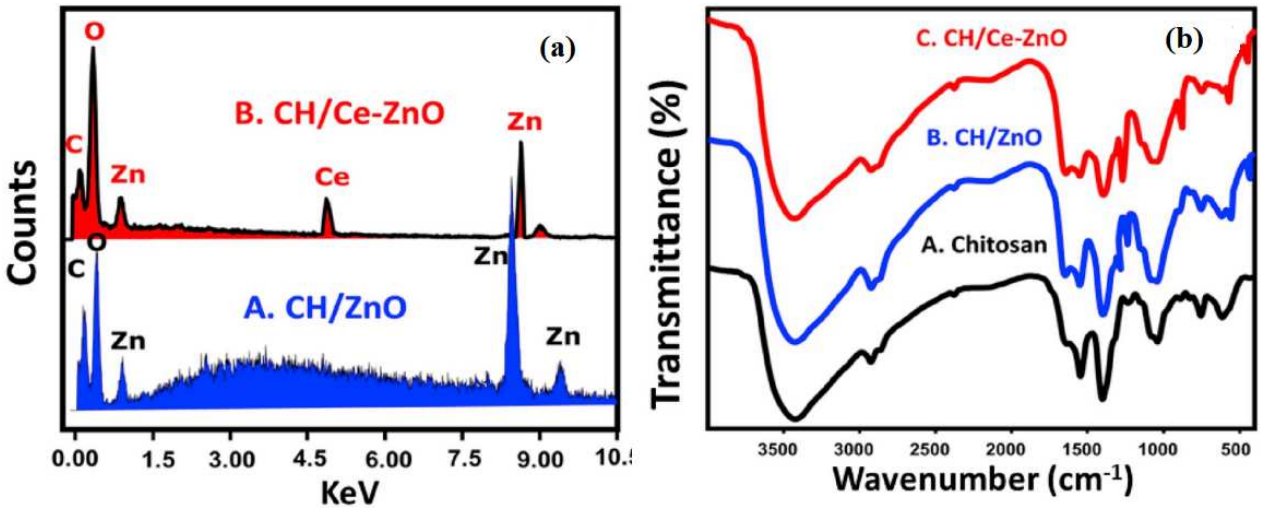

Figure 15. EDX spectra (**a**) and FTIR spectra (**b**) of ZnO/chitosan (CH) and Ce–ZnO/CH [103].

Saad et al. [103] reported the synthesis of chitosan supported the ZnO and Ce–ZnO nanoflowers. The EDX and FT-IR study (Figure 15) confirmed the formation of the ma-

terials. Changes in chemical composition and surface functional groups determine each material's adsorption capacity and properties. Chitosan is an organic compound that contains functional groups such as OH, N-H, C-H, C-N, and C-O, which were observed in the IR spectra of the composites. The observed spectral band changes, such as the increased intensities of the OH-related absorption bands, confirmed the loading of ZnO and Ce-ZnO onto the chitosan. The EDX analysis showed that the ZnO/chitosan sample contains C, O, and Zn, whereas, in addition, the Ce–ZnO/chitosan composite incorporated Ce (Figure 15a). Furthermore, the band at 564 cm^{-1} in the FT-IR data (Figure 15b) also confirmed the presence of the Zn-O-Ce group [106].

4. Techniques for Improving the Performance of ZnO Materials in Catalysis

ZnO is a cheap semiconductor material with excellent electrical and mechanical antifouling [122], antibacterial, and optical properties [123]. The ideal modified ZnO-based photocatalyst aims to improve its efficiency and extend its application in the visible region for practical applications. It also includes the ease of upgrading catalyst systems for large-scale industrial and municipal applications and high recyclability without a loss in activity [124]. Therefore, many modifications have been proposed and executed to obtain the desired ideal ZnO photocatalyst. Some of the more common modifications are highlighted in the following sections [61,125,126].

4.1. Doping with Metals

The ZnO lattice can be doped with transition metals due to similarities between the ionic radii of Zn^{2+} and other transition metal ions with unfilled *d*-subshells; hence, the possibility of the movement of the charges between the *d* subshells of the metal ions and the conduction or valence band of ZnO [95]. The result is a new electronic state in the band gap of ZnO by energy reduction. The (TPDT/(ZnO-Ag) materials prepared by Praveen et al. [82] are good examples. The materials were fabricated by the deposition of Ag nanoparticles onto ZnO nanoparticles spread in a silicate sol-gel matrix to form a hybrid catalyst for the photodegradation of organic pollutants. In the system, the OH^-/H_2O couple traps the photoinduced ZnO holes to produce reactive $^{\bullet}OH$, an oxidant radical for the degradation of pollutant molecules [127]. The Ag nanoparticles (charge sink) on the ZnO also enhanced the interfacial delivery of the charges to break down pollutant molecules, thereby reducing the band gap energy [128]. The enhanced photocatalysis indicated that the materials' efficiency is due to the amine-functionalised TPDT matrix. Similarly, the same strategy was used to develop heterostructures with excellent abilities to remove dyes. The energy band gap of the photocatalysts was reduced to 1.7, 2.7, and 2.8 eV for ZnO-Cu (**S1**), ZnO-Ag (**S2**), and ZnO-Au (**S3**), respectively. The band-gap energy reduction may be associated with the new band level in the ZnO semiconductor surface due to doping with Cu, Ag, and Au transition metals. However, in the presence of radical scavengers, such as methanol or propan-2-ol, the degradation rate was reduced, indicating the involvement of hydroxyl radicals in the photodegradation, which was confirmed by benzoic acid hydroxylation, and the GC-MS detection of hydroquinone during the degradation of phenol [83].

4.2. Coupling of Semiconductors

Raj et al. [57] coupled MgO/ZnO semiconductors to improve the practical application of ZnO for the degradation of colourant molecules. The multi-component system showed improvement by preventing the recombination of photoinduced charge carriers. In the photocatalyst's heterojunction, electrons are trapped in the conduction band of MgO (narrow band gap), while the positive charges are restricted in the valence band of ZnO (wide band gap). Furthermore, a shift in the spectral response into the Vis region ($\geq$400 nm) and reduced band gap energy (lower than the parent semiconductors) enhanced the photocatalytic efficiency of the hybrid material.

The BiOCl/ZnO p-n heterojunctions fabricated by Chang et al. [61] with exposed crystals of the (101) surfaces are stimulated by Vis irradiation, which is better than a

previous [129] attempt that only absorbed in the UV region of the spectrum. The superior photocatalytic activity was ascribed to the enhanced Vis absorption of BiOCl, larger surface area, and the built-in potential from the p-n junctions of BiOCl/ZnO, as illustrated in Figure 16.

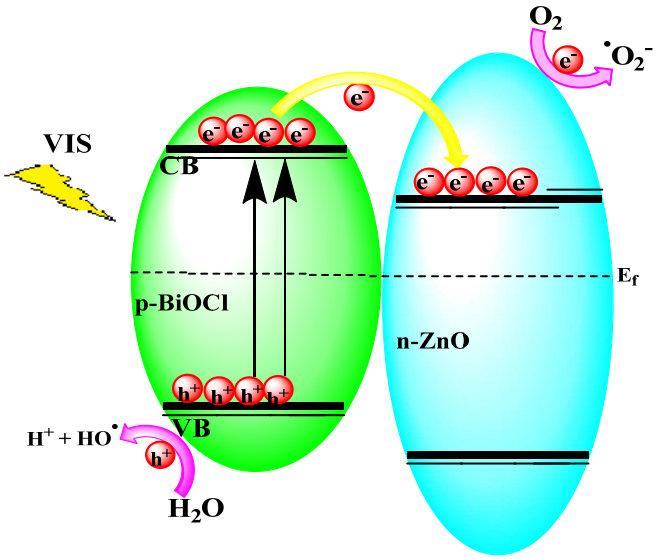

Figure 16. Mechanisms of degradation by BiOCl/ZnO p-n heterojunction materials [61].

4.3. Coupling with Carbon Materials

The mineralisation of the safranin-T dye on the surface of the functionalised GO nanosheets (FGS) was achieved by an attack of reactive species that included h^+, $O_2^{-\bullet}$, and $^\bullet$OH (Figure 17). This was induced by the direct irradiation and oxidation of the dye adsorbed on the surface of the material enabled by photogenerated holes on its valence band via p-p interactions. On the other hand, the electrons were transmitted efficiently to the FGS from the ZnO. Their strong interaction hampered the recombination of the e^-/h^+ charges. In addition, the $O_2^{\bullet-}$ radicals were produced from the combination of electrons on the photocatalyst surface and trapped dissolved oxygen to further the degradation of the dye molecules via an $^\bullet$OH radical attack [130].

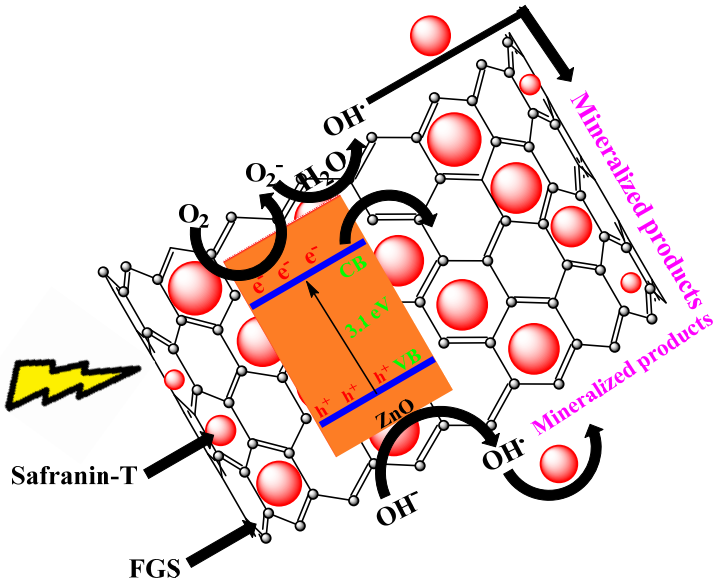

Figure 17. Illustration of the degradation of safranin-T dye by FGS/ZnO materials [130].

4.4. Immobilised Photocatalysts

A suitable photocatalyst support must permanently immobilise the catalyst, have a large surface area, and increase catalyst activity upon immobilisation. Desirable characteristics of an immobilising material include the ability to adsorb the catalyst and absorb sufficient light energy for effective activity and also be robustly stable to withstand the degenerative impact of the strong oxidative radicals generated during photocatalysis.

Cold plasma discharge, RF magnetron sputtering, dip coating, polymer-assisted hydrothermal decomposition, photo etching, spray pyrolysis, electrophoretic deposition, and spray pyrolysis are some examples of common immobilisation methods [23]. Most catalyst supports are porous materials with high specific surface areas and electronic configurations that induce interactions with the catalyst that produce slightly acidic conditions for efficient electron transfer, hence mitigating e^-/h^+ recombination. Commonly used supports include glass substrates, zeolites, alumina, carbon [80,81], and carbon-covered alumina (CCA) [131]. In particular, CCA is a support system that exploits the qualities of both carbon and alumina and, therefore, provides a model support system [92].

Velanganni et al. [132] used SILAR to fabricate a fluorine-doped tin-oxide glass deposited with Bi_2S_3/ZnO. The process involved three steps with 20 cycles of immersion in a series of solutions. Once constituted, the supported thin-film catalysts degraded 91% of methylene blue under Vis irradiation. In addition, Baradaran and Ghodsi [133] used the binder-less approach to fabricate a superior third-generation photocatalyst. The heteromorphic zinc oxide/aluminium-doped zinc oxide/zinc oxide (ZnO/AZO/ZnO) composite was deposited by spin-coating on a glass substrate. The synthesised heteromorphs exhibited high transmittance (>80%) in the Vis region, confirming the response shift. The crystallite size of the photocatalysts decreased with an increase in the thickness of the ZnO:Al couple. This multi-layered fabricated system prevented the recombination of photoinduced charges. Under Vis irradiation, the concentration of •OH radicals increased, resulting in the effective photolysis of the methylene blue dye, which is better than with either ZnO or ZnO/AZO [133].

Furthermore, Tsai et al. [134] fabricated Cu_2O and Ag nanoparticle-decorated ZnO nanorods on a flexible, lightweight, cheap paper. It was an easy-to-produce Vis-active photocatalyst for pollutant degradation. The hydrothermal technique was used to grow the ZnO nanorods, followed by the photoreduction processes (a binder-less process) to produce a Kraft paper decorated with either Cu_2O, Ag, or both nanoparticles. The Kraft paper was successfully used to degrade rhodamine B dye under Vis and sunlight.

5. Further Details on Applications of the ZnO Nanomaterials in Photocatalysis

One of the main objectives of this review was to assess the use of ZnO nanoparticles as a basis for the generation of photoactive Vis catalysts in general wastewater treatment and dye removal from wastewater, in particular. Most important are the highlights presented herein on recent alterations successfully used to improve the photodegradation of organic dyes. Most of the ZnO nanostructured materials discussed thus far are second- or third-generation photocatalysts. The applications of the key ones are collected in Table 7 for ease of reference and are further discussed below.

Table 7. Removal efficiency of ZnO nanoparticles in dyes polluted wastewater treatments.

S/N	Material (Dosage)	Dye (Conc.)	Efficiency	Affected Material Properties	Ref.
1	Fe-Cu-ZnO/GO (1 g)	Dark green Dye (50 ppm)	99% in 90 min	Pollutant removal efficiency by enhanced adsorption due to Cu & Fe doping & large specific surface area due GO, efficient charge separation.	[56]
2	ZnO/MgO (100 mg)	Textile dyeing (50 mL)	65% in 120 min	Small particle size, reduced band gap.	[57]

Table 7. *Cont.*

S/N	Material (Dosage)	Dye (Conc.)	Efficiency	Affected Material Properties	Ref.
3	Cd:Ag:ZnO: PVP (30 mg)	MB (20 ppm)	99% in 120 min	Reduced band gap, good charge transfer and reduced charge recombination	[60]
4	BiOCl/ZnO (50 mg)	RhB (10 ppm)	100% in 15 min	charge separation by heterojunction.	[61]
5	La-ZnO-GO (100 mg)	EY (20 ppm)	100% in 210 min	Pollutant removal efficiency by enhanced enhanced VIS response due to La doping & large specific surface area due GO, efficient charge separation.	[75]
6	ZnO-embedded S-doped g-C_3N_4 (50 mg)	MB and RhB (10 ppm)	93% 80 min	Enhanced visible light response and charge separation behaviour.	[76]
7	ZnO/g-C_3N_4 (25 mg)	Congo red (10 ppm)	100% in 120 min	Reduced band gap.	[77]
8	ZnO/Fe_3O_4/g-C_3N_4 (10 mg)	MO, AYR, & OG (30 ppm)	98%, 98%, & 83% in 150 min respectively	Charge separation efficiency by heterojunction.	[78]
9	$AgIO_4$/ZnO (100 mg).	RhB (2×10^{-5} M) & IC (5×10^{-5} M) dyes	81% of RhB & 98% of IC in 120 min	Reduction in band gap	[79]
10	TPDT/(ZnO-Ag) 20 mg	MB, Cr(iv) (1.5×10^{-5} M)	100% in 60 min	Charge separation efficiency by heterojunction	[82]
11	Cu/Ag/Au-loaded ZnO (20 mg)	Various phenolic dyes (100 ppm)	100% in 180 min	Band gap dependent on metal-exchange capacity, doped metals improves VIS response & reduced charge recombination.	[83]
12	ZnO/GO (100 mg)	Ciprofloxacin MB, MG, EY, (25 ppm)	100%, 100%, 98%, 87% in 180 min	Increase active sites due to GO, reduced charge recombination, reduced band gap all of which improve photocatalytic performance	[84]
13	CuO/ZnO (50 mg)	MB (10 ppm)	97% in 25 min	p–n junction, reduced charge recombination	[86]
14	Ag/ZnO (500 mg)	RB5 (1.0×10^{-5} M)	72% in 780 min	Plasmonic effect	[87]
15	g-C_3N_4-ZnO@graphene (5 mg)	RhB, MV, MO (20 ppm)	83% 150 min	Pollutant removal efficiency by synergy btw adsorption & photocatalysis, charge separation by heterojunction.	[93]
16	g-C_3N_4/ZnO (50 mg)	RhB	92% in 120 min	good charge transfer & reduced charge recombination.	[94]
17	Cu-ZnO (50 mg)	MO (0.02 mM)	100% in 150 min	good charge transfer & reduced charge recombination	[95]
18	ZnO-Ag_8S (1×1 cm^2 thin film)	RhB (1×10^{-3} M)	7.3 times better than ZnO	electron trapping which hindered the charge carrier recombination	[96]
19	$ZnFe_2O_4$/Ag-ZnO (50 mg)	RhB (10 ppm)	100% in 300 min	good charge transfer & reduced charge recombination	[97]
20	C-ZnO/$BiVO_4$ (75 mg)	MB (10 ppm)	100% in 50 min	Doping, heterojunction, surface defect traps charges control recombination	[98]
21	Ce–ZnO/Chitosan (20 mg)	MG (5 ppm)	87% in 90 min	Reduction in band gap	[103]
22	ZnO/polypyrrole (50 mg)	AV 7 (5 ppm)	64% in 360 min	band gap indeterminable, but high VIS shift.	[104]
23	ZnO and g-C_3N_4 (1 g)	MB & RhB (10 ppm)	97% MB in 50 min	Enhanced charge separation and visible light response.	[108]
24	ZnO/g-C_3N_4/Ag (Thin film)	MB & MG (1×10^{-5} M)	96% & 99% in 90 min	Reduced band gap & reduced charge recombination.	[110]
25	FGS/ZnO (20 mg).	Safranin T (2.2×10^{-4} M)	95% in 90 min	Dye removal efficiency by enhanced adsorption due to FGS & efficient charge separation	[130]

Table 7. *Cont.*

S/N	Material (Dosage)	Dye (Conc.)	Efficiency	Affected Material Properties	Ref.
26	Bi_2S_3/ZnO (Thin film)	MB (20 ppm)	92% in 200 min	Charge separation efficiency by heterojunction	[132]
27	ZnO/AZO/ZnO (Thin film)	MB (30 mg)	95% in 180 min	Smaller crystallite size, surface defect, results in efficient separation of e/h pairs.	[133]

Abbreviations: EY—eosin yellow; MO—methyl orange; MV—methyl violet; RhB—Rhodamine B; OG—orange G; MB—methylene blue; MG—malachite green; IC—indigo carmine; AYR—alizarin yellow R.

5.1. Graphitic Carbon Nitride (gC_3N_4) and Organic Doped Materials

Graphite, carbon fibre, carbon nanotube, graphene, carbon black, activated carbon, fullerene, and others are all carbon materials. Carbon as a support material has good interactions with the metals they support, a neutral surface, good thermal conductivity, and a large surface area with a tuneable pore volume with many surface functional groups [92]. Amongst the second-generation catalysts, coupling ZnO with graphitic carbon nitride (gC_3N_4) is one of the most common procedures in enhancing Vis absorption and, ultimately, photocatalytic activity. Graphitic carbon nitride with a band gap energy of 2.65 eV is cheap, easy to produce, and attractive to researchers. In addition, it is a two-dimensional structural material with excellent chemical stability and a tuneable electronic structure. g-C_3N_4 embedded with ZnO reduces its band gap energy and enhances the Vis degradation of dyes (Z-scheme system results in Vis active materials). The study by Kalisamy et al. [76] reported a heterojunction composite ZnO-embedded S-doped g-C_3N_4 with an efficiency of up to a 93% removal of methylene blue and rhodamine B dyes in 80 min. The composite was stable up till the fifth cycle of reuse. This was achieved due to the high speed of hydroxyl radical production via the improved separation of e^-/h^+ in the ZnO nanocarbon material. The study also compared the band gap energies of g-C_3N_4, ZnO, and ZnO/g-C_3N_4 materials as 2.66 eV, 3.2 eV, and 2.63 eV, respectively, revealing the impact of the heterojunction on the band gap energy. In a related study, Shemeena and Binitha reported that 25 mg of a ZnO/g-C_3N_4 successfully degraded 10 mg/L of Congo red dye at 100% in 50 min [77]. Wu et al. [78] took it even further with their ternary ZnO/Fe_3O_4/g-C_3N_4 material (combination of three nanomaterials), which attained a 98% degradation efficiency of 30 mg/L of alizarin yellow R in 150 min.

Similarly, Zhang et al. [93] applied a g-C_3N_4-ZnO@GA (g-C_3N_4-ZnO@graphene aerogel) nanocarbon material in photocatalysis. The study demonstrated that the Z-scheme heterojunction catalyst degraded rhodamine B dye under UV (81%) and Vis (83%) irradiation. The g-C_3N_4-ZnO@GA (30%) catalytic activity was due to the hierarchical porous nature of the material and the beneficial synergistic impact among the components that combined to contribute to its effectiveness [93]. Additionally, the pompon-like structured g-C_3N_4/ZnO composite prepared by Zhang et al. [94], which comprises flakes of g-C_3N_4 coated on the ZnO surface, degraded 92% of rhodamine B dye in 2 h at a catalyst loading of 10%. The study concluded that superoxide and hydroxyl radicals are the main reactive species driving photocatalysis [94].

5.2. Heterojunction Semiconductor and Metal-Doped Materials

In exploiting the benefits of a heterojunction between semiconductors, as enumerated earlier, Sarmah et al. [83] reported that the presence of CuO on ZnO enhanced its absorption in the Vis region and utilised the photo-generated electron of the $Cu^{I/0}$ reduction process, thereby preventing e^-/h^+ recombination, hence improving the photocatalytic performance of the material. Similarly, a MgO/ZnO heterojunction improved the ZnO degradation of colourant molecules. The shift in its spectral response into the Vis spectrum and reduced band gap energy (lower than the individual semiconductors) enhanced the photocatalyst efficiency [57]. Additionally, BiOCl/ZnO p-n heterojunctions with exposed crystals of the (101) surface are stimulated by Vis irradiation. The nanocarbon material completely

degraded rhodamine B dye in 15 min [64]. In another study, the heterojunction in the $AgIO_4$/ZnO composite has electrons restricted in the $AgIO_4$ conduction band (transferred from ZnO) and the positive charges confined in the ZnO valence band. This separation of the photoinduced charges overpowers their recombination, thus generating active sites for dye molecule degradation. Abdel-Aziz et al. [79] reported that the nanoparticle under sunlight irradiation degraded 98% of indigo carmine and 81% of rhodamine B dyes in 110 min. The high performance of the $AgIO_4$/ZnO material is likely due to superoxide radicals being the main active dye mineralisation species.

Similarly, Venugopal et al. [96] synthesised a ZnO-Ag_8S hybrid for the photocatalytic degradation of dyes. The ZnO-Ag_8S hybrid nanoparticle with simultaneous piezophototronic effect efficiently degraded rhodamine B dye. In addition, the study reported a seven-fold increment in the ZnO-Ag_8S photocatalytic performance compared with the pristine ZnO [96]. A further merit of heterojunction materials was observed with the $ZnFe_2O_4$/Ag–ZnO composite, which exhibited surface plasmon resonance in the Vis region due to the Ag ions. The nanodiscs synthesised by Karunakaran et al. [97] completely degraded rhodamine B in 300 min under Vis irradiation and showed good reusability with little or no activity loss.

The Z-scheme junction between C-ZnO and $BiVO_4$ overcame all the inherent shortcomings of the parent semiconductors. Hence, an efficient C-ZnO/$BiVO_4$ heterostructured nanocarbon material with enhanced photocatalytic performance was obtained. The strategy resulted in the better degradation of rhodamine B in 50 min, a result that is a significant improvement on pure ZnO under Vis irradiation [98]. A related strategy was based on TiO_2-modified ZnO for photocatalysis, in which the photoactivity and photostability of the ZnO were also improved for the degradation of rhodamine B and methyl orange dyes [32]. Raj et al. [57], Bharathi et al. [86], and Santos et al. [87] prepared ZnO-based photocatalysts using wet-chemical methods. All the catalysts successfully degraded pollutant dyes. The ZnO/MgO nanomaterial achieved good photocatalysis by degrading 65% of textile dye wastewater in 120 min under Vis irradiation with excellent antibacterial properties. The improved catalytic activity may not be unconnected to the reduced particle size and band gap energy. Additionally, 50 mg of the CuO/ZnO nanomaterial degraded 97% of 10 ppm of methylene blue in 25 min under Vis irradiation. In contrast, 0.50 g of the Ag/ZnO degraded 10^{-5} M of the reactive black 5 dye in 780 min. The observed improved activity of the heterogeneous photocatalyst was attributed to the plasmonic Ag in its composition [135]. It is important to state that there was no modification to the band gap energy [87].

Doping of ZnO with metals changes the chemical surroundings of the Zn atom and tunes its electronic structure. For example, Gaurav et al. prepared Cu ion-doped ZnO nanomaterials and determined their optical band gap energy (as low as 3.11). The reduction in the band gap energy was primarily due to the electronic structure modification that led to 99.5% photodegradation of methyl orange dye by 1% of the Cu-doped ZnO catalyst under sunlight irradiation in 150 min [95].

5.3. Graphene Oxide, Mesoporous and Polymeric Material-Modified Catalysts

Taking advantage of the unique properties of graphene oxide, Zhu et al. [56] prepared Fe-Cu-ZnO/graphene oxide composites with good adsorption properties. They utilised the dual properties of adsorption and photodegradation in dye removal from water. The study reported that a dose of 1g of the composite catalyst degraded 99% of 50 mg/L of dark green organic dyes under Vis irradiation. The study noted that the effect might be due to two factors: firstly, Fe and Cu doping shifted the spectral response of ZnO to the Vis region and served as traps for the photoinduced charge carriers at appropriate doping levels, effectively separating them, thereby prolonging the lifetime of hydroxyl radicals. Secondly, with its high specific surface area, graphene oxide improved the movement of the electrons, efficiently increasing the light-harvesting ability and dye adsorption, contributing to an enhanced photocatalytic degradation efficiency. A Vis-active La-doped ZnO/graphene oxide composite material was synthesised by Oppong et al. [75]. The

improved photocatalysis of the composite was due to the graphene oxide behaving as an electron scavenger preventing the recombination of the charge carriers. The material also displayed good reusability and stability with a photocatalytic performance of 98% compared to 18% for pure ZnO material under similar simulated solar light irradiation conditions [75]. A similar study by Zarrabi et al. [84] prepared ZnO/graphene oxide to study the effects of sonication and the graphene oxide support on the structural and dynamic features of the photocatalyst. They reported that the incorporation of graphene oxide aided the movement of the electrons from the ZnO, preventing the recombination of the photogenerated charges (e^-/h^+). The report also revealed that 0.1 g of the material as a photocatalyst degraded 98–100% of 25 ppm of the dye pollutants methylene blue, malachite green, and eosin yellow in 180 min [84].

Other related research works with mesoporous materials include the synthesis of ZnO nanoparticles decorated with amino silicate sol-gel matrix-supported Ag nanoparticles [TPDT/(ZnO-Ag)] for the removal of toxic methylene blue and Cr (VI) for environmental remediation by Praveen et al. [82]. They reported that the Ag nanoparticles on ZnO further enhanced the interfacial electron transfer rate of the pollutant molecules; hence, the catalyst successfully degraded the methylene blue dye in 60 min. In addition, chitosan/Ce–ZnO composites exhibited improved photocatalytic activities under Vis irradiation, with 0.02g of the material degrading 100% of 5 mg/L of the malachite green dye after 90 min. The time was reduced to 60 min when 0.03g of the catalyst was used. The study reported that the photogenerated e^-/h^+ pairs and the $^{\bullet}OH$ radicals are the primary active-charged species. The study also reported a reduction in band gap energies from 3.3 eV (ZnO) to 2.85 eV for the Ce–ZnO composite and further to 2.5 eV for the chitosan/Ce–ZnO [103].

Polymeric materials have also been adopted as supports. For the polyvinylpyrrolidone-capped Cd, Ag-doped ZnO nanomaterials fabricated by Vignesh et al. [60] using a microwave synthesis method, it was revealed that the enhanced photocatalytic activity was due to a decreased band gap energy attributed to Sn and Cu ions doping into the ZnO framework. This is due to sp↔d orbital exchange interactions, enabling the effective interfacial charge transfer and suppressing the recombination of the separated charge carriers. Hence, 100 mg of the materials degraded 99% of 20 mg/L of methylene blue within 180 min. The related study by González-Casamachin et al. [104] on polypyrrole-supported (ZnO/PPy) composite materials exploited the properties of PPy, including its good electrical and optical features, high absorption coefficients, high mobility of photoinduced charges, and excellent stability to improve the catalytic performance of ZnO. Under Vis irradiation, 50 mg of the composite degraded 64% of 5ppm of the acid violet 7 dye in a continuous annular reactor.

Finally, to overcome the problems inherent in first- and second-generation photocatalysts, the binder-through and binder-less methods were used to immobilise the earlier-generation photocatalysts onto different substrates. However, the latter approach is the method of choice due to the apparent problems of using chemicals in water treatment and the hydrophilicity of the binders [136]. Third-generation photocatalyst materials provide a viable solution to postseparation problems [136]. The binder-less method Baradaran and Ghodsi [133] used to deposit ZnO/AZO/ZnO composites on glass resulted in a layered system that degraded 95% of 30 mg/L of methylene blue in 180 min, better than ZnO or ZnO/AZO under Vis irradiation. Similarly, the Kraft paper deposited with Cu_2O and Ag nanoparticle-decorated ZnO nanorods degraded 10 μM of rhodamine B dye in 80 min of Vis and sunlight irradiation [134].

6. Conclusions and Prospects

The most important goal for future investigation is to develop greener methods for synthesising ZnO-based photocatalysts. In addition, the following are areas for future consideration for ZnO photocatalysis:

- Despite the numerous reports on ZnO nanoparticles with different morphologies, many desirable enhancements to important properties (such as the crystallinity and sphericity of the particles) are required for improved photocatalytic performance.

- More photocatalysis research should use pollutants of concern instead of just model compounds. In recent works, dyes were used as models for organic pollutants in photocatalytic degradation studies. However, many dyes (containing known chromophores) are easier to degrade than persistent organic compounds such as pesticides, pharmaceuticals, and organ disruptors.
- A more fundamental understanding of the mineralisation pathways at the interface between the photocatalyst and the contaminant is still desired.
- Operational problems need to be addressed. These include the poor recovery of photocatalysts during post-treatment work-up and its impact on the photoactivity of the recycled catalyst. The problem also extends to catalysts dispersed as powders and the reduction in the activity of immobilised/supported photocatalysts on subsequent runs.
- Finally, there is a need for theoretical tools in developing new photocatalysts. Meta-analytic studies will cut down on waste by trial and error, which is common in many of today's research endeavours.

Various factors hamper the use of photocatalysis for water clean-up on a broader scale. The most important considerations are pricing and the pressing demand for innovative TiO_2 alternatives. This article has presented an up-to-date investigation of ZnO nanostructured materials. A detailed survey on strategies for altering the properties of ZnO nanoparticles to improve their adaptability as photocatalysts was presented. Decolouration of water was generally used as the model reaction, partly because reliable spectroscopic data are easily generated by monitoring the degradation of coloured dyes in aqueous solutions. Although ZnO nanostructured materials are promising candidates as photocatalysts for the Vis-driven photodegradation of recalcitrant organic impurities, fresh strategies are needed to surmount the incessant bottlenecks encountered while using pure, unmodified ZnO in photocatalytic processes. As detailed in several sections of this article, the fabrication methods used affect the photocatalyst morphology, particle size, and usability. ZnO nanoparticles prepared by various methods, including sol-gel, wet-chemical, hydrothermal, and synthetic solvothermal techniques, exhibited greater than 90% degradation of various dye pollutants within short irradiation periods. Simpler solution-based approaches are generally preferred to the more exotic microwave, ultrasonic/hydrothermal, and precipitation/sono-precipitation fabrication methods. The sol-gel method proved an effective synthetic path based on pricing, simplicity, and reliability. Hence, the preferred process for effectively controlling important nanoparticle properties, such as uniformity in particle size, eventually leads to better photocatalytic efficiency.

Additionally, the band-gap energy level is essential in defining the catalytic activity of ZnO in dye degradation and other applications. Synthetic strategies to suppress the speed of charge carrier recombination are better at improving the photocatalytic efficiencies of new photocatalyst materials. Such endeavours are better than those aimed at band-gap reduction as the primary aim. Therefore, procedures such as metal/non-metal doping, ZnO coupling with other semiconductors, and coupling with carbon materials enhanced the photocatalytic efficiency of ZnO in photodegradation applications.

Finally, the types of semiconductor coupling materials, the relative quantity of the dopants, and the relative position of their band gap energies are factors of interest to be considered to optimise the photoactivity of ZnO materials. These considerations shift the band gap energy (by shifting the photoresponse of the catalyst to the Vis region), inhibiting the recombination of the photoinduced e^-/h^+ charges, thereby improving the separation efficiency. Eventually, more research is required to generate new, unique supporting agents that will overcome the intrinsic mass transfer constraints of immobilised ZnO-based photocatalysts for upscaling to large-scale industrial and municipal operations beyond current laboratory explorations.

Author Contributions: Conceptualization, A.D.F. and M.D.B.; methodology, A.D.F. and M.D.B.; formal analysis, A.D.F. and M.D.B.; investigation, A.D.F.; resources, M.D.B.; data curation, A.D.F. and M.D.B.; writing—original draft preparation, A.D.F.; writing—review and editing, M.D.B.; supervision, M.D.B.; project administration, M.D.B.; funding acquisition, M.D.B. All authors have read and agreed to the published version of the manuscript.

Funding: The authors thank ESKOM (TESP 2021) and the National Research Foundation (South Africa) (No. 145775) for financial support.

Conflicts of Interest: The authors declare that they have no known competing financial interest or personal relationship that could have appeared to influence the work reported in this paper.

References

1. Rajasulochana, P.; Preethy, V. Comparison on the efficiency of various techniques in the treatment of waste and sewage water–A comprehensive review. *Resour.-Effic. Technol.* **2016**, *2*, 175–184. [CrossRef]
2. Markham, A.C. *A Brief History of Pollution*; Routledge: London, UK, 2019.
3. Zeng, G.; Chen, M.; Zeng, Z. Risks of neonicotinoid pesticides. *Science* **2013**, *340*, 1403. [CrossRef] [PubMed]
4. Değermenci, G.D.; Değermenci, N.; Ayvaoğlu, V.; Durmaz, E.; Çakır, D.; Akan, E. Adsorption of reactive dyes on lignocellulosic waste; characterization, equilibrium, kinetic and thermodynamic studies. *J. Clean. Prod.* **2019**, *225*, 1220–1229. [CrossRef]
5. Banaei, A.; Samadi, S.; Karimi, S.; Vojoudi, H.; Pourbasheer, E.; Badiei, A. Synthesis of silica gel modified with 2, 2′-(hexane-1, 6-diylbis (oxy)) dibenzaldehyde as a new adsorbent for the removal of Reactive Yellow 84 and Reactive Blue 19 dyes from aqueous solutions: Equilibrium and thermodynamic studies. *Powder Technol.* **2017**, *319*, 60–70. [CrossRef]
6. Moussavi, G.; Mahmoudi, M. Removal of azo and anthraquinone reactive dyes from industrial wastewaters using MgO nanoparticles. *J. Hazard. Mater.* **2009**, *168*, 806–812. [CrossRef]
7. Shimada, C.; Kano, K.; Sasaki, Y.F.; Sato, I.; Tsuda, S. Differential colon DNA damage induced by azo food additives between rats and mice. *J. Toxicol. Sci.* **2010**, *35*, 547–554. [CrossRef]
8. Walthall, W.K.; Stark, J.D. The acute and chronic toxicity of two xanthene dyes, fluorescein sodium salt and phloxine B, to Daphnia Pulex. *Environ. Pollut.* **1999**, *104*, 207–215. [CrossRef]
9. Oturan, M.A.; Aaron, J.-J. Advanced Oxidation Processes in Water/Wastewater Treatment: Principles and Applications. A Review. *Crit. Rev. Environ. Sci. Technol.* **2014**, *44*, 2577–2641. [CrossRef]
10. Ajmal, A.; Majeed, I.; Malik, R.N.; Idriss, H.; Nadeem, M.A. Principles and mechanisms of photocatalytic dye degradation on TiO_2 based photocatalysts: A comparative overview. *RSC Adv.* **2014**, *4*, 37003–37026. [CrossRef]
11. Attour, A.; Ben Grich, N.; Mouldi Tlili, M.; Ben Amor, M.; Lapicque, F.; Leclerc, J.P. Intensification of phosphate removal using electrocoagulation treatment by continuous pH adjustment and optimal electrode connection mode. *Desalination Water Treat.* **2016**, *57*, 13255–13262. [CrossRef]
12. Tang, X.; Zheng, H.; Teng, H.; Sun, Y.; Guo, J.; Xie, W.; Yang, Q.; Chen, W. Chemical coagulation process for the removal of heavy metals from water: A review. *Desalination Water Treat.* **2016**, *57*, 1733–1748. [CrossRef]
13. G Gallego-Urrea, J.A.; Hammes, J.; Cornelis, G.; Hassellöv, M. Coagulation and sedimentation of gold nanoparticles and illite in model natural waters: Influence of initial particle concentration. *NanoImpact* **2016**, *3*, 67–74. [CrossRef]
14. Charles, J.; Bradu, C.; Morin-Crini, N.; Sancey, B.; Winterton, P.; Torri, G.; Badot, P.M.; Crini, G. Pollutant removal from industrial discharge water using individual and combined effects of adsorption and ion-exchange processes: Chemical abatement. *J. Saudi Chem. Soc.* **2016**, *20*, 185–194. [CrossRef]
15. Wang, D.K.; Elma, M.; Motuzas, J.; Hou, W.-C.; Xie, F.; Zhang, X. Rational design and synthesis of molecular-sieving, photocatalytic, hollow fiber membranes for advanced water treatment applications. *J. Membr. Sci.* **2017**, *524*, 163–173. [CrossRef]
16. Pype, M.-L.; Lawrence, M.G.; Keller, J.; Gernjak, W. Reverse osmosis integrity monitoring in water reuse: The challenge to verify virus removal—A review. *Water Res.* **2016**, *98*, 384–395. [CrossRef]
17. Dickhout, J.M.; Moreno, J.; Biesheuvel, P.; Boels, L.; Lammertink, R.G.; de Vos, W.M. Produced water treatment by membranes: A review from a colloidal perspective. *J. Colloid Interface Sci.* **2017**, *487*, 523–534. [CrossRef]
18. Subramani, A.; Jacangelo, J.G. Emerging desalination technologies for water treatment: A critical review. *Water Res.* **2015**, *75*, 164–187. [CrossRef]
19. Munoz, I.; Rodriguez, A.; Rosal, R.; Fernandez-Alba, A.R. Life cycle assessment of urban wastewater reuse with ozonation as tertiary treatment: A focus on toxicity-related impacts. *Sci. Total Environ.* **2009**, *407*, 1245–1256. [CrossRef]
20. Miranda, A.C.; Lepretti, M.; Rizzo, L.; Caputo, I.; Vaiano, V.; Sacco, O.; Lopes, W.S.; Sannino, D. Surface water disinfection by chlorination and advanced oxidation processes: Inactivation of an antibiotic resistant *E. coli* strain and cytotoxicity evaluation. *Sci. Total Environ.* **2016**, *554*, 1–6. [CrossRef]
21. Taka, A.L.; Pillay, K.; Mbianda, X.Y. Nanosponge cyclodextrin polyurethanes and their modification with nanomaterials for the removal of pollutants from waste water: A review. *Carbohydr. Polym.* **2017**, *159*, 94–107. [CrossRef]
22. Muhd Julkapli, N.; Bagheri, S.; Bee Abd Hamid, S. Recent advances in heterogeneous photocatalytic decolorization of synthetic dyes. *Sci. World J.* **2014**, *2014*, 692307. [CrossRef] [PubMed]

23. Srikanth, B.; Goutham, R.; Badri Narayan, R.; Ramprasath, A.; Gopinath, K.P.; Sankaranarayanan, A.R. Recent advancements in supporting materials for immobilised photocatalytic applications in waste water treatment. *J. Environ. Manag.* **2017**, *200*, 60–78. [CrossRef]
24. Sleiman, M.; Vildozo, D.; Ferronato, C.; Chovelon, J.M. Photocatalytic degradation of azo dye Metanil Yellow: Optimization and kinetic modelling using a chemometric approach. *Appl. Catal. B* **2007**, *77*, 1–11. [CrossRef]
25. Whipple, D.T.; Kenis, P.J.A. Prospects of CO_2 Utilization via Direct Heterogeneous Electrochemical Reduction. *J. Phys. Chem. Lett.* **2010**, *1*, 3451–3458. [CrossRef]
26. Rochkind, M.; Pasternak, S.; Paz, Y. Using Dyes for Evaluating Photocatalytic Properties: A Critical Review. *Molecules* **2015**, *20*, 88–110. [CrossRef] [PubMed]
27. Vinodgopal, K.; Bedja, I.; Hotchandani, S.; Kamat, P.V. A Photocatalytic Approach for the Reductive Decolorization of Textile Azo Dyes in Colloidal Semiconductor Suspensions. *Langmuir* **1994**, *10*, 1767–1771. [CrossRef]
28. Shu, H.M.; Xie, J.M.; Xu, H.; Li, H.M.; Gu, Z.; Sun, G.S.; Xu, Y.G. Structural characterization and photocatalytic activity of $NiO/AgNbO_3$. *J. Alloys Compd.* **2010**, *496*, 633–637. [CrossRef]
29. Shaham-Waldmann, N.; Paz, Y. Away from TiO_2: A critical minireview on the developing of new photocatalysts for degradation of contaminants in water. *Mater. Sci. Emicond. Process.* **2016**, *42*, 72–80. [CrossRef]
30. Tian, C.; Zhang, Q.; Wu, A.; Jiang, M.; Liang, Z.; Jiang, B.; Fu, H. Cost-effective large-scale synthesis of ZnO photocatalyst with excellent performance for dye photodegradation. *Chem. Commun.* **2012**, *48*, 2858–2860. [CrossRef]
31. Chang, C.J.; Chu, K.W.; Hsu, M.H.; Chen, C.Y. Ni-doped ZnS decorated graphene composites with enhanced photocatalytic hydrogen-production performance. *Int. J. Hydrogen Energy* **2015**, *40*, 14498–14506. [CrossRef]
32. Ruíz-Santoyo, V.; Marañon-Ruiz, V.F.; Romero-Toledo, R.; González Vargas, O.A.; Pérez-Larios, A. Photocatalytic degradation of Rhodamine B and methylene orange using TiO_2-ZrO_2 as nanocomposite. *Catalysts* **2021**, *11*, 1035. [CrossRef]
33. Zeng, Z.; Xu, Y.; Zhang, Z.; Gao, Z.; Luo, M.; Yin, Z.; Zhang, C.; Xu, J.; Huang, B.; Luo, F.; et al. Rare-earth-containing perovskite nanomaterials: Design, synthesis, properties and applications. *Chem. Soc. Rev.* **2020**, *49*, 1109–1143. [CrossRef]
34. Li, Z.; Meng, X.; Zhang, Z. Recent development on MoS_2-based photocatalysis: A review. *J. Photochem. Photobiol. C* **2018**, *35*, 39–55. [CrossRef]
35. Sayama, K.; Hayashi, H.; Arai, T.; Yanagida, M.; Gunji, T.; Sugihara, H. Highly active WO_3 semiconductor photocatalyst prepared from amorphous peroxo-tungstic acid for the degradation of various organic compounds. *Appl. Catal. B* **2010**, *94*, 150–157. [CrossRef]
36. Li, Q.; Li, X.; Wageh, S.; Al-Ghamdi, A.A.; Yu, J.G. CdS/Graphene Nanocomposite Photocatalysts. *Adv. Energy Mater.* **2015**, *5*, 1500010. [CrossRef]
37. Mahadik, M.; Shinde, S.; Mohite, V.; Kumbhar, S.; Rajpure, K.; Moholkar, A.; Kim, J.; Bhosale, C. Photoelectrocatalytic oxidation of Rhodamine B with sprayed α-Fe_2O_3 photocatalyst. *Mater. Express* **2013**, *3*, 247–255. [CrossRef]
38. Periyat, P.; Pillai, S.C.; McCormack, D.E.; Colreavy, J.; Hinder, S.J. Improved high-temperature stability and sun-light-driven photocatalytic activity of sulfur-doped anatase TiO_2. *J. Phys. Chem. C* **2008**, *112*, 7644–7652. [CrossRef]
39. Afzaal, M.; Malik, M.A.; O'Brien, P. Preparation of zinc containing materials. *New J. Chem* **2007**, *31*, 2029–2040. [CrossRef]
40. Sun, B.; Sirringhaus, H. Solution-processed zinc oxide field-effect transistors based on self-assembly of colloidal nanorods. *Nano Lett.* **2005**, *5*, 2408–2413. [CrossRef]
41. Ellmer, K.; Klein, A.; Rech, B. *Transparent Conductive Zinc Oxide: Basics and Applications in Thin Film Solar Cells*; Springer Science & Business Media: Berlin/Heidelberg, Germany, 2007.
42. Lee, C.R.; Lee, H.W.; Song, J.S.; Kim, W.W.; Park, S. Synthesis and Ag recovery of nanosized ZnO powder by solution combustion process for photocatalytic applications. *J. Mater. Synth. Process.* **2001**, *9*, 281–286. [CrossRef]
43. Dodd, A.C.; McKinley, A.J.; Saunders, M.; Tsuzuki, T. Effect of particle size on the photocatalytic activity of nanoparticulate zinc oxide. *J. Nanopart. Res.* **2006**, *8*, 43–51. [CrossRef]
44. Klingshirn, C. ZnO: Material, physics and applications. *Chemphyschem* **2007**, *8*, 782–803. [CrossRef] [PubMed]
45. Qi, K.; Cheng, B.; Yu, J.; Ho, W. Review on the improvement of the photocatalytic and antibacterial activities of ZnO. *J. Alloys Compd.* **2017**, *727*, 792–820. [CrossRef]
46. Fenoll, J.; Ruiz, E.; Hellin, P.; Flores, P.; Navarro, S. Heterogeneous photocatalytic oxidation of cyprodinil and fludioxonil in leaching water under solar irradiation. *Chemosphere* **2011**, *85*, 1262–1268. [CrossRef] [PubMed]
47. Chen, W.; Lu, W.; Yao, Y.; Xu, M. Highly efficient decomposition of organic dyes by aqueous-fiber phase transfer and in situ catalytic oxidation using fiber-supported cobalt phthalocyanine. *Environ. Sci. Technol.* **2007**, *41*, 6240–6245. [CrossRef]
48. Lucilha, A.C.; Bonancêa, C.E.; Barreto, W.J.; Takashima, K. Adsorption of the diazo dye Direct Red 23 onto a zinc oxide surface: A spectroscopic study. *Spectrochim. Acta A Mol. Biomol. Spectrosc.* **2010**, *75*, 389–393. [CrossRef] [PubMed]
49. Wan, Q.; Wang, T.H.; Zhao, J.C. Enhanced photocatalytic activity of ZnO nanotetrapods. *Appl. Phys. Lett.* **2005**, *87*, 083105:1–083105:4. [CrossRef]
50. Bauer, C.; Boschloo, G.; Mukhtar, E.; Hagfeldt, A. Electron injection and recombination in $Ru(dcbpy)_2(NCS)_2$ sensitized nanostructured ZnO. *J. Phys. Chem. B* **2001**, *105*, 5585–5588. [CrossRef]
51. Fattakhova-Rohlfing, D.; Zaleska, A.; Bein, T. Three-dimensional titanium dioxide nanomaterials. *Chem. Rev.* **2014**, *11*, 9487–9558. [CrossRef]
52. Blencowe, D.K.; Morby, A.P. Zn (II) metabolism in prokaryotes. *FEMS Microbiol. Rev.* **2003**, *27*, 291–311. [CrossRef]

53. Ong, C.B.; Ng, L.Y.; Mohammad, A.W. A review of ZnO nanoparticles as solar photocatalysts: Synthesis, mechanisms and applications. *Renew. Sust. Energy Rev.* **2018**, *81*, 536–551. [CrossRef]
54. Sun, W.; Zhang, S.; Liu, Z.; Wang, C.; Mao, Z. Studies on the enhanced photocatalytic hydrogen evolution over Pt/PEG-modified TiO_2 photocatalysts. *Int. J. Hydrogen Energy* **2008**, *33*, 1112–1117. [CrossRef]
55. Macak, J.M.; Sirotna, K.; Schmuki, P. Self-organized porous titanium oxide prepared in Na_2SO_4/NaF electrolytes. *Electrochim. Acta* **2005**, *50*, 3679–3684. [CrossRef]
56. Zhu, P.F.; Chen, Y.J.; Duan, M.; Liu, M.; Zou, P.; Zhou, M. Enhanced visible photocatalytic activity of Fe-Cu-ZnO/graphene oxide photocatalysts for the degradation of organic dyes. *Can. J. Chem. Eng.* **2018**, *96*, 1479–1488. [CrossRef]
57. Raj, R.B.; Umadevi, M.; Parimaladevi, R. Enhanced photocatalytic degradation of textile dyeing wastewater under UV and visible light using ZnO/MgO nanocomposites as a novel photocatalyst. *Part. Sci. Technol.* **2020**, *38*, 812–820. [CrossRef]
58. Das, D.; Nandi, P. Ternary ZnCdSO composite photocatalyst for efficient dye degradation under visible light retaining Z-scheme of migration pathways for the photogenerated charge carriers. *Sol. Energy Mater. Sol. Cells* **2020**, *217*, 110674. [CrossRef]
59. Sabri, M.; Habibi-Yangjeh, A.; Ghosh, S. Novel ZnO/$CuBi_2O_4$ heterostructures for persulfate-assisted photocatalytic degradation of dye contaminants under visible light. *J. Photochem. Photobiol. A* **2020**, *391*, 112397:1–112397:11. [CrossRef]
60. Vignesh, S.; Suganthi, S.; Sundar, J.K.; Raj, V.; Devi, P.R.I. Highly efficient visible light photocatalytic and antibacterial performance of PVP capped Cd:Ag: ZnO photocatalyst nanocomposites. *Appl. Surf. Sci.* **2019**, *479*, 914–929. [CrossRef]
61. Chang, J.-Q.; Zhong, Y.; Hu, C.-H.; Luo, J.-L.; Wang, P.-G. Study on highly efficient BiOCl/ZnO pn heterojunction: Synthesis, characterization and visible-light-excited photocatalytic activity. *J. Mol. Struct.* **2019**, *1183*, 209–216. [CrossRef]
62. Cao, F.; Pan, Z.H.; Ji, X.H. Enhanced photocatalytic activity of a pine-branch-like ternary CuO/CuS/ZnO heterostructure under visible light irradiation. *New J. Chem.* **2019**, *43*, 11342–11347. [CrossRef]
63. Lee, S.J.; Jung, H.J.; Koutavarapu, R.; Lee, S.H.; Arumugam, M.; Kim, J.H.; Choi, M.Y. ZnO supported Au/Pd bimetallic nanocomposites for plasmon improved photocatalytic activity for methylene blue degradation under visible light irradiation. *Appl. Surf. Sci.* **2019**, *496*, 143665. [CrossRef]
64. Ouyang, W.; Zhu, J. Catalyst-free synthesis of macro-scale ZnO nanonail arrays on Si substrate by simple physical vapor deposition. *Mater. Lett.* **2008**, *62*, 2557–2560. [CrossRef]
65. Wang, C.Z.; Chen, Z.; Hu, H.Q.; Zhang, D. Effect of the oxygen pressure on the microstructure and optical properties of ZnO films prepared by laser molecular beam epitaxy. *Phys. B Condens. Matter* **2009**, *404*, 4075–4082. [CrossRef]
66. Behnajady, M.A.; Modirshahla, N.; Ghazalian, E. Synthesis of ZnO nanoparticles at different conditions: A comparison of photocatalytic activity. *Dig. J. Nanomater. Biostructures* **2011**, *6*, 467–474.
67. Zhou, K.; Zhang, Q.; Shi, Y.; Jiang, S.; Hu, Y.; Gui, Z. A facile method for preparation ZnO with different morphology and their optical property. *J. Alloys Compd.* **2013**, *577*, 389–394. [CrossRef]
68. Tsay, C.-Y.; Fan, K.-S.; Lei, C.-M. Synthesis and characterization of sol–gel derived gallium-doped zinc oxide thin films. *J. Alloys Compd.* **2012**, *512*, 216–222. [CrossRef]
69. Burda, C.; Chen, X.; Narayanan, R.; El-Sayed, M.A. Chemistry and properties of nanocrystals of different shapes. *Chem. Rev.* **2005**, *105*, 1025–1102. [CrossRef] [PubMed]
70. Akhtar, K.; Zubair, N.; Ikram, S.; Khan, Z.U.; Khalid, H. Synthesis and characterization of ZnO nanostructures with varying morphology. *Bull. Mater. Sci.* **2017**, *40*, 459–466. [CrossRef]
71. Gupta, J.; Barick, K.; Bahadur, D. Defect mediated photocatalytic activity in shape-controlled ZnO nanostructures. *J. Alloys Compd.* **2011**, *509*, 6725–6730. [CrossRef]
72. Zhang, J.; Sun, L.; Yin, J.; Su, H.; Liao, C.; Yan, C. Control of ZnO Morphology via a Simple Solution Route. *Chem. Mater.* **2002**, *14*, 4172–4177. [CrossRef]
73. Ramakrishna, G.; Ghosh, H.N. Effect of particle size on the reactivity of quantum size ZnO nanoparticles and charge-transfer dynamics with adsorbed catechols. *Langmuir* **2003**, *19*, 3006–3012. [CrossRef]
74. Selvin, S.S.P.; Radhika, N.; Borang, O.; Lydia, I.S.; Merlin, J.P. Visible light driven photodegradation of Rhodamine B using cysteine capped ZnO/GO nanocomposite as photocatalyst. *J. Mater. Sci. Mater. Electron.* **2017**, *28*, 6722–6730. [CrossRef]
75. Oppong, S.O.B.; Anku, W.W.; Opoku, F.; Shukla, S.K.; Govender, P.P. Photodegradation of Eosin Yellow Dye in Water under Simulated Solar Light Irradiation Using La-Doped ZnO Nanostructure Decorated on Graphene Oxide as an Advanced Photocatalyst. *ChemistrySelect* **2018**, *3*, 1180–1188. [CrossRef]
76. Kalisamy, P.; Lallimathi, M.; Suryamathi, M.; Palanivel, B.; Venkatachalam, M. ZnO-embedded S-doped gC_3N_4 heterojunction: Mediator-free Z-scheme mechanism for enhanced charge separation and photocatalytic degradation. *RSC Adv.* **2020**, *10*, 28365–28375. [CrossRef]
77. Shemeena, M.; Binitha, N.N. Visible light active ZnO-g-C_3N_4 photocatalyst for dye pollutant degradation. *Mater.-Proc.* **2020**, *25*, 107–110. [CrossRef]
78. Wu, Z.; Chen, X.; Liu, X.; Yang, X.; Yang, Y. A ternary magnetic recyclable ZnO/Fe_3O_4/gC_3N_4 composite photocatalyst for efficient photodegradation of monoazo dye. *Nanoscale Res. Lett* **2019**, *14*, 147. [CrossRef]
79. Abdel-Aziz, R.; Ahmed, M.A.; Abdel-Messih, M.F. A novel UV and visible-light-driven photocatalyst $AgIO_4$/ZnO nanoparticles with highly enhanced photocatalytic performance for removal of rhodamine B and indigo carmine dyes. *J. Photochem. Photobiol. C* **2020**, *389*, 112245. [CrossRef]

80. Liu, S.-H.; Wei, Y.-S.; Lu, J.-S. Visible-light-driven photodegradation of sulfamethoxazole and methylene blue by Cu_2O/rGO photocatalysts. *Chemosphere* **2016**, *154*, 118–123. [CrossRef]
81. Moradi, M.; Haghighi, M.; Allahyari, S. Precipitation dispersion of Ag–ZnO nanocatalyst over functionalized multiwall carbon nanotube used in degradation of Acid Orange from wastewater. *Process. Saf. Environ. Prot.* **2017**, *107*, 414–427. [CrossRef]
82. Praveen, R.; Chandreshia, C.B.; Ramaraj, R. Silicate sol-gel matrix stabilized ZnO-Ag nanocomposites materials and their environmental remediation applications. *J. Environ. Chem. Eng.* **2018**, *6*, 3702–3708. [CrossRef]
83. Sarmah, K.; Roy, U.K.; Maji, T.K.; Pratihar, S. Role of Metal Exchange toward the Morphology and Photocatalytic Activity of Cu/Ag/Au-Doped ZnO: A Study with a Zinc-Sodium Acetate Complex as the Precursor. *ACS Appl. Nano Mater.* **2018**, *1*, 2049–2056. [CrossRef]
84. Zarrabi, M.; Haghighi, M.; Alizadeh, R.; Mahboob, S. Solar-light-driven photodegradation of organic dyes on sono-dispersed ZnO nanoparticles over graphene oxide: Sono vs. conventional catalyst design. *Sep. Purif. Technol.* **2019**, *211*, 738–752. [CrossRef]
85. Saleem, H.; Haneef, M.; Abbasi, H.Y. Synthesis route of reduced graphene oxide via thermal reduction of chemically exfoliated graphene oxide. *Mater. Chem. Phys.* **2018**, *204*, 1–7. [CrossRef]
86. Bharathi, P.; Harish, S.; Archana, J.; Navaneethan, M.; Ponnusamy, S.; Muthamizhchelvan, C.; Shimomura, M.; Hayakawa, Y. Enhanced charge transfer and separation of hierarchical CuO/ZnO composites: The synergistic effect of photocatalysis for the mineralization of organic pollutant in water. *Appl. Surf. Sci.* **2019**, *484*, 884–891. [CrossRef]
87. Santos, P.B.; Santos, J.J.; Correa, C.C.; Corio, P.; Andrade, G.F.S. Plasmonic photodegradation of textile dye Reactive Black 5 under visible light: A vibrational and electronic study. *J. Photochem. Photobiol. A* **2019**, *371*, 159–165. [CrossRef]
88. Das, A.; Wary, R.R.; Nair, R.G. Cu modified ZnO nanoflakes: An efficient visible light-driven photocatalyst and a promising photoanode for dye sensitized solar cell (DSSC). *Solid State Sci.* **2020**, *104*, 106290. [CrossRef]
89. Peter, C.N.; Anku, W.W.; Sharma, R.; Joshi, G.M.; Shukla, S.K.; Govender, P.P. N-doped ZnO/graphene oxide: A photostable photocatalyst for improved mineralization and photodegradation of organic dye under visible light. *Ionics* **2019**, *25*, 327–339. [CrossRef]
90. Selvaraj, S.; Mohan, M.K.; Navaneethan, M.; Ponnusamy, S.; Muthamizhchelvan, C. Synthesis and photocatalytic activity of Gd doped ZnO nanoparticles for enhanced degradation of methylene blue under visible light. *Mater. Sci. Semicond. Process.* **2019**, *103*, 104622. [CrossRef]
91. Chen, X.; Mao, S.S. Titanium dioxide nanomaterials: Synthesis, properties, modifications, and applications. *Chem. Rev.* **2007**, *107*, 2891–2959. [CrossRef]
92. Mahlambi, M.M.; Ngila, C.J.; Mamba, B.B. Recent developments in environmental photocatalytic degradation of organic pollutants: The case of titanium dioxide nanoparticles—A review. *J. Nanomater.* **2015**, *2015*, 790173. [CrossRef]
93. Zhang, J.Y.; Mei, J.Y.; Yi, S.S.; Guan, X.X. Constructing of Z-scheme 3D g-C_3N_4-ZnO@graphene aerogel heterojunctions for high-efficient adsorption and photodegradation of organic pollutants. *Appl. Surf. Sci.* **2019**, *492*, 808–817. [CrossRef]
94. Zhang, B.; Li, M.; Wang, X.; Zhao, Y.; Wang, H.; Song, H. Pompon-like structured gC_3N_4/ZnO composites and their application in visible light photocatalysis. *Res. Chem. Intermed.* **2018**, *44*, 6895–6906. [CrossRef]
95. Gaurav, A.; Beura, R.; Kumar, J.S.; Thangadurai, P. Study on the effect of copper ion doping in zinc oxide nanomaterials for photocatalytic applications. *Mater. Chem. Phys.* **2019**, *230*, 162–171. [CrossRef]
96. Venugopal, G.; Thangavel, S.; Vasudevan, V.; Zoltan, K. Efficient visible-light piezophototronic activity of ZnO-Ag_8S hybrid for degradation of organic dye molecule. *J. Phys. Chem. Solids* **2020**, *143*, 109473. [CrossRef]
97. Karunakaran, C.; JebaSing, I.; Vinayagamoorthy, P. Synthesis of Superparamagnetic $ZnFe_2O_4$-Core/Ag-Deposited ZnO-Shell Nanodiscs for Application as Visible Light Photocatalyst. *J. Nanosci. Nanotechnol.* **2019**, *19*, 4064–4071. [CrossRef]
98. Srinivasan, N.; Anbuchezhiyan, M.; Harish, S.; Ponnusamy, S. Hydrothermal synthesis of C doped ZnO nanoparticles coupled with $BiVO_4$ and their photocatalytic performance under the visible light irradiation. *Appl. Surf. Sci* **2019**, *494*, 771–782. [CrossRef]
99. Tofa, T.S.; Ye, F.; Kunjali, K.L.; Dutta, J. Enhanced Visible Light Photodegradation of Microplastic Fragments with Plasmonic Platinum/Zinc Oxide Nanorod Photocatalysts. *Catalysts* **2019**, *9*, 819. [CrossRef]
100. Bharti, D.B.; Bharati, A.V. Photocatalytic degradation of Alizarin Red dye under visible light using ZnO & CdO nanomaterial. *Optik* **2018**, *160*, 371–379. [CrossRef]
101. Cheng, Y.; Wang, W.Z.; Yao, L.Z.; Wang, J.; Liang, Y.J.; Fu, J.L. Insights into charge transfer and solar light photocatalytic activity induced by the synergistic effect of defect state and plasmon in Au nanoparticle-decorated hierarchical 3D porous ZnO microspheres. *Appl. Surf. Sci.* **2019**, *494*, 959–968. [CrossRef]
102. Manjunatha, C.; Abhishek, B.; Shivaraj, B.; Ashoka, S.; Shashank, M.; Nagaraju, G. Engineering the M_x Zn_{1-x} O (M= Al^{3+}, Fe^{3+}, Cr^{3+}) nanoparticles for visible light-assisted catalytic mineralization of methylene blue dye using Taguchi design. *Chem. Zvesti* **2020**, *74*, 2719–2731. [CrossRef]
103. Saad, A.M.; Abukhadra, M.R.; Ahmed, S.A.K.; Elzanaty, A.M.; Mady, A.H.; Betiha, M.A.; Shim, J.J.; Rabie, A.M. Photocatalytic degradation of malachite green dye using chitosan supported ZnO and Ce-ZnO nano-flowers under visible light. *J. Environ. Manag.* **2020**, *258*, 110043. [CrossRef] [PubMed]
104. González-Casamachin, D.A.; De la Rosa, J.R.; Lucio-Ortiz, C.J.; De Rio, D.A.D.H.; Martínez-Vargas, D.X.; Flores-Escamilla, G.A.; Guzman, N.E.D.; Ovando-Medina, V.M.; Moctezuma-Velazquez, E. Visible-light photocatalytic degradation of acid violet 7 dye in a continuous annular reactor using ZnO/PPy photocatalyst: Synthesis, characterization, mass transfer effect evaluation and kinetic analysis. *Chem. Eng. J.* **2019**, *373*, 325–337. [CrossRef]

105. Fouda, A.; Salem, S.S.; Wassel, A.R.; Hamza, M.F.; Shaheen, T.I. Optimization of green biosynthesized visible light active CuO/ZnO nano-photocatalysts for the degradation of organic methylene blue dye. *Heliyon* **2020**, *6*, e04896-1. [CrossRef]
106. Ullah, H.; Mushtaq, L.; Ullah, Z.; Fazal, A.; Khan, A.M. Effect of vegetable waste extract on microstructure, morphology, and photocatalytic efficiency of ZnO-CuO nanocomposites. *Inorg. Nano-Met. Chem.* **2021**, *51*, 963–975. [CrossRef]
107. Reddy, I.N.; Reddy, C.V.; Shim, J.; Akkinepally, B.; Cho, M.Y.; Yoo, K.; Kim, D. Excellent visible-light-driven photocatalyst of (Al, Ni) co-doped ZnO structures for organic dye degradation. *Catal. Today* **2020**, *340*, 277–285. [CrossRef]
108. Prabhu, S.; Pudukudy, M.; Harish, S.; Navaneethan, M.; Sohila, S.; Murugesan, K.; Ramesh, R. Facile construction of djembe-like ZnO and its composite with g-C_3N_4 as a visible-light-driven heterojunction photocatalyst for the degradation of organic dyes. *Mater. Sci. Semicond. Process.* **2020**, *106*, 104754. [CrossRef]
109. Sapkota, K.P.; Lee, I.; Hanif, M.A.; Islam, M.A.; Hahn, J.R. Solar-light-driven efficient ZnO–single-walled carbon nanotube photocatalyst for the degradation of a persistent water pollutant organic dye. *Catalysts* **2019**, *9*, 498. [CrossRef]
110. Ravichandran, K.; Sindhuja, E. Fabrication of cost-effective g-C_3N_4 $^+$Ag activated ZnO photocatalyst in thin-film form for enhanced visible light-responsive dye degradation. *Mater. Chem. Phys.* **2019**, *221*, 203–215. [CrossRef]
111. Lonkar, S.P.; Pillai, V.V.; Alhassan, S.M. Facile and scalable production of heterostructured ZnS-ZnO/Graphene nano-photocatalysts for environmental remediation. *Sci. Rep.* **2018**, *8*, 13401. [CrossRef]
112. Meng, Q.M.; Lu, Q.L.; Wang, L.X.; Wang, J. Fe-doped ZnO synthesized by parallel flow precipitation process for improving photocatalytic activity. In *IOP Conference Series: Materials Science and Engineering, Proceedings of the 2nd International Conference on New Material and Chemical Industry (NMCI2017), Sanya, China, 18–20 November 2017*; IOP Publishing Ltd.: Bristol, UK, 2018; Volume 292, p. 012065. [CrossRef]
113. Worathitanon, C.; Jangyubol, K.; Ruengrung, P.; Donphai, W.; Klysubun, W.; Chanlek, N.; Prasitchoke, P.; Chareonpanich, M. High-performance visible-light responsive Chl-Cu/ZnO catalysts for photodegradation of rhodamine B. *Appl. Catal. B* **2019**, *241*, 359–366. [CrossRef]
114. Özgür, Ü.; Alivov, Y.I.; Liu, C.; Teke, A.; Reshchikov, M.; Doğan, S.; Avrutin, V.C.S.J.; Cho, S.J.; Morkoç, A.H. A comprehensive review of ZnO materials and devices. *J. Appl. Phys.* **2005**, *98*, 11. [CrossRef]
115. Manzoor, U.; Kim, D.K. Size control of ZnO nanostructures formed in different temperature zones by varying Ar flow rate with tunable optical properties. *Phys. E Low Dimens. Syst. Nanostruct.* **2009**, *41*, 500–505. [CrossRef]
116. Ginley, D.S.; Perkins, J.D. Transparent conductors. In *Handbook of Transparent Conductors*; Springer: Boston, MA, USA, 2011; pp. 1–25.
117. Claflin, B.; Look, D.C.; Park, S.-J.; Cantwell, G. Persistent n-type photoconductivity in p-type ZnO. *J. Cryst. Growth* **2006**, *287*, 16–22. [CrossRef]
118. Yang, C.; Kwack, Y.; Kim, S.H.; An, T.K.; Hong, K.; Nam, S.; Park, M.; Choi, W.S.; Park, C.E. Ambipolar thin-film transistors and an inverter based on pentacene/self-assembled monolayer modified ZnO hybrid structures for balanced hole and electron mobilities. *Org. Electron.* **2011**, *12*, 411–418. [CrossRef]
119. Tsukazaki, A.; Ohtomo, A.; Onuma, T.; Ohtani, M.; Makino, T.; Sumiya, M.; Ohtani, K.; Chichibu, S.F.; Fuke, S.; Segawa, Y.; et al. Repeated temperature modulation epitaxy for p-type doping and light-emitting diode based on ZnO. *Nat. Mater.* **2005**, *4*, 42–46. [CrossRef]
120. Mourdikoudis, S.; Pallares, R.M.; Thanh, N.T. Characterization techniques for nanoparticles: Comparison and complementarity upon studying nanoparticle properties. *Nanoscale* **2018**, *10*, 12871–12934. [CrossRef]
121. Shanmugam, V.; Jeyaperumal, K.S. Investigations of visible-light-driven Sn and Cu doped ZnO hybrid nanoparticles for photocatalytic performance and antibacterial activity. *Appl. Surf. Sci.* **2018**, *449*, 617–630. [CrossRef]
122. Al-Fori, M.; Dobretsov, S.; Myint, M.T.Z.; Dutta, J. Antifouling properties of zinc oxide nanorod coatings. *Biofouling* **2014**, *30*, 871–882. [CrossRef]
123. Gharoy Ahangar, E.; Abbaspour-Fard, M.H.; Shahtahmassebi, N.; Khojastehpour, M.; Maddahi, P. Preparation and characterization of PVA/ZnO nanocomposite. *J. Food Process. Preserv.* **2015**, *39*, 1442–1451. [CrossRef]
124. Kuo, W.; Ho, P. Solar photocatalytic decolourization of methylene blue in water. *Chemosphere* **2001**, *45*, 77–83. [CrossRef]
125. Khan, M.T.; Chatterjee, D.; Bala, M. Photocatalytic reduction of N_2 to NH_3 sensitized by the [RuIII-ethylenediaminetetraacetate-2, 2′-bipyridyl]−complex in a Pt-TiO_2 semiconductor particulate system. *J. Photochem. Photobiol. A* **1992**, *67*, 349–352. [CrossRef]
126. Borjigin, B.; Ding, L.; Li, H.; Wang, X. A solar light-induced photo-thermal catalytic decontamination of gaseous benzene by using Ag/Ag_3PO_4/CeO_2 heterojunction. *Chem. Eng. J.* **2020**, *402*, 126070. [CrossRef]
127. Deng, Q.; Tang, H.; Liu, G.; Song, X.; Xu, G.; Li, Q.; Ng, D.H.; Wang, G. The fabrication and photocatalytic performances of flower-like Ag nanoparticles/ZnO nanosheets-assembled microspheres. *Appl. Surf. Sci.* **2015**, *331*, 50–57. [CrossRef]
128. Subramanian, V.; Wolf, E.; Kamat, P.V. Semiconductor−metal composite nanostructures. To what extent do metal nanoparticles improve the photocatalytic activity of TiO_2 films? *J. Phys. Chem. B* **2001**, *105*, 11439–11446. [CrossRef]
129. Li, Y.-F.; Zhang, M.; Guo, D.-L.; He, F.-X.; Li, Y.-Z.; Wang, A.-J. Facile solvothermal synthesis of BiOCl/ZnO heterostructures with enhanced photocatalytic activity. *J. Nanomater.* **2014**, *2014*, 347061. [CrossRef]
130. Nenavathu, B.P.; Kandula, S.; Verma, S. Visible-light-driven photocatalytic degradation of safranin-T dye using functionalized graphene oxide nanosheet (FGS)/ZnO nanocomposites. *RSC Adv.* **2018**, *8*, 19659–19667. [CrossRef] [PubMed]

131. Mahlambi, M.M.; Mishra, A.K.; Mishra, S.B.; Krause, R.W.; Mamba, B.B.; Raichur, A.M. Synthesis and characterization of carbon-covered alumina (CCA) supported TiO_2 nanocatalysts with enhanced visible-light photodegradation of Rhodamine B. In *Nanotechnology for Sustainable Development*; Springer: Berlin/Heidelberg, Germany, 2012; pp. 89–99. [CrossRef]
132. Velanganni, S.; Manikandan, A.; Prince, J.J.; Mohan, C.N.; Thiruneelakandan, R. Nanostructured ZnO coated Bi_2S_3 thin films: Enhanced photocatalytic degradation of methylene blue dye. *Phys. B Condens. Matter* **2018**, *545*, 383–389. [CrossRef]
133. Baradaran, M.; Ghodsi, F.E. Highly efficient visible photocatalytic degradation of MB organic dye by heteromorphic ZnO/AZO/ZnO nanocatalysts: Effect of AZO thickness. *J. Sol-Gel Sci. Technol.* **2019**, *92*, 25–39. [CrossRef]
134. Tsai, C.-E.; Yeh, S.-M.; Chen, C.-H.; Lin, H.-N. Flexible photocatalytic paper with Cu_2O and Ag nanoparticle-decorated ZnO nanorods for visible light photodegradation of organic dye. *Nanoscale Res. Lett.* **2019**, *14*, 204. [CrossRef]
135. Wu, N. Plasmonic metal–semiconductor photocatalysts and photoelectrochemical cells: A review. *Nanoscale* **2018**, *10*, 2679–2696. [CrossRef]
136. Anwer, H.; Mahmood, A.; Lee, J.; Kim, K.-H.; Park, J.-W.; Yip, A.C.K. Photocatalysts for degradation of dyes in industrial effluents: Opportunities and challenges. *Nano Res.* **2019**, *12*, 955–972. [CrossRef]